6

Particle Identification

6.1 Physics Requirement and Performance Goals

6.1.1 Introduction

Excellent particle identification for hadrons and leptons over a large range of solid angle and momentum is an essential requirement for meeting the physics objectives of BaBar. In particular, measurements of CP violation require particle identification, both to reconstruct exclusive final states and to tag the quark content of the other B in the event. Information from the drift chamber, calorimeter, and the instrumented flux return can be used to identify most of the leptons and many of the hadrons. However, these systems are not sufficient to distinguish charged pions from kaons with momenta greater than about $0.7\,\mathrm{GeV}/c$, or protons above $1.3\,\mathrm{GeV}/c$, as is required to obtain efficient tagging and event reconstruction. To meet these requirements, dedicated particle identification will be provided by a combination of Cherenkov counters: a ring-imaging detector in the barrel region (the DIRC, for Detection of Internally Reflected Cherenkov light) and a threshold detector in the forward endcap region (the ATC, for Aerogel Threshold Cherenkov counter) with two indices of refraction. No dedicated particle identification in the backward region is needed.

6.1.2 B Flavor Tagging

The flavor of B mesons will primarily be tagged with charged kaons and leptons: a b-quark decay leads to a K^- and/or a direct lepton ℓ^-, and a $\overline{b}$-quark decay leads to a K^+ and/or a direct lepton ℓ^+. B-flavor tagging thus relies on the identification of kaons and leptons in an environment of inclusive B decays with large multiplicities of low-momentum daughters, where relative abundances of pions, kaons, and protons are approximately 7:1:0.2. Because of the boost ($\beta\gamma = 0.56$), the average $\pi(K)$ momentum depends on the polar angle, and

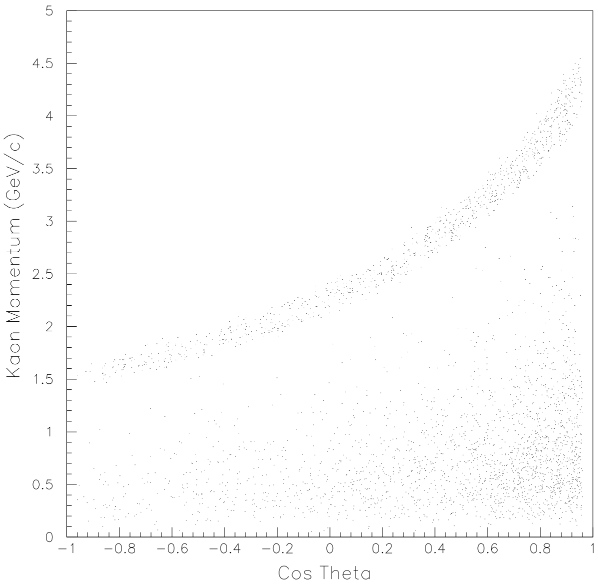

Figure 6-1. *Inclusive momentum spectrum for kaons as a function of polar angle in the laboratory frame. The banded region is an enhanced population of kaons from the decay $B \rightarrow K\pi$.*

ranges from about 0.3(0.45) GeV/c in the backward direction to about 0.75(1.1) GeV/c in the forward direction.

The effective tagging efficiency is defined as $\epsilon_{eff} = \epsilon_{tag} \times (1 - 2w)^2$, where ϵ_{tag} is the fraction of tagged B events, and w is the fraction of tagged events which are incorrect. The effective efficiency is limited by physics itself, for example, by wrong-sign contamination from Cabibbo-suppressed decays or from kaon or lepton pairs. In the case of kaon tagging, even assuming perfect particle identification and no kaon decays in flight, the maximum tagging rates and minimum wrong-tag fractions which can be achieved within the *BABAR* acceptance are 36.3% and 6.6%, respectively. This leads to a maximum effective efficiency of 27.3%. Kaon decays result in a further 20% reduction of efficiency. The loss of efficiency introduced by the PID system must be small in comparison. Given the relative abundances noted above, a small misidentification rate for pions is particularly crucial.

The measurement of ionization in the drift chamber will provide π/K separation better than 3σ up to 0.7 GeV/c, but will be of limited assistance in the relativistic rise region at higher momenta. As a consequence, the dE/dx measurement is not itself sufficient, since 48% of all kaons would remain untagged, as demonstrated by the momentum distribution shown in Figure 6-1.

Kaon tagging thus requires dedicated PID systems that achieve high efficiency and purity. Furthermore, because the forward region subtends a large fraction of the center-of-mass solid angle, tagging efficiency is sensitive to the forward PID coverage. In the proposed design, the DIRC covers 86.5% of the full solid angle, down to $\theta = 445\,\mathrm{mr}$, and, combined with dE/dx, provides an effective tagging efficiency of 18.5%. The very forward part ($300 < \theta < 412\,\mathrm{mr}$) covered by the ATC represents 5% of the full solid angle, and a dedicated PID system in this region, in combination with dE/dx, increases the effective tagging efficiency by 3.4% to 19.1%. To make this contribution, the forward aerogel needs to be able to tag kaons up to 1.5–2 GeV/c through the use of an aerogel layer with an index of refraction $n = 1.055$.

In the case of lepton tagging, the dE/dx measurement ensures electron identification over the full momentum spectrum. However, muon identification by range measurement in the flux return is efficient only above about 0.7 GeV/c. At lower momenta, the DIRC, primarily designed for its π/K separation capabilities, will also provide μ/π separation, complementary to the IFR.

6.1.3 Exclusive B decays

The search for CP-violating modes, such as $B^0 \to \pi^+\pi^-$ or $B^0 \to \rho\pi$, and the measurement at much higher momentum of V_{ub} through charmless B decays, places greater demands on the performance of the PID system than those required for tagging. The exclusive branching ratios of interest are very small (10^{-5}), and CP violation studies are made even more challenging by the need to tag the other B in $\Upsilon(4S) \to B^0\overline{B}^0$ decays. While much of the background from the continuum can be suppressed by simple kinematic cuts, the reduction of correlated backgrounds from $B^0 \to \pi^+K^-$, $B^0 \to \rho K$, and $B^0 \to K^*(892)\pi$ demands that pions be positively identified, with a minimum of kaon misidentification, in the high-momentum range up to 3–4.5 GeV/c. Non-B physics will also be demanding in terms of kaon identification. A challenging example is the study of rare strange decays of the tau lepton in which the momentum spectrum is very hard (up to 8 GeV/c).

An example of a detailed analysis of a two-body mode requiring high-momentum particle identification is given in Chapter 3. A study of the decay $B^0 \to \pi^+\pi^-$ is reported which relies on the combination of DIRC and ATC to suppress the correlated $K^+\pi^-$ background. These ASLUND studies show that dE/dx and kinematics, while providing significant capability for identification of the $B^0 \to \pi^+\pi^-$ exclusive channel, are not sufficient to guarantee both high efficiency and low background. Requiring a reasonable separation between the competing mass hypotheses, *e.g.,* by demanding that the χ^2 for the $\pi^+\pi^-$ assignment exceeds alternatives by at least four, quickly reduces acceptances from 92% to 80% in the case of idealized particle tracking and dE/dx performance; accounting for reasonable degradation in the actual running detector lowers these estimates to unacceptable levels. The addition of the DIRC/ATC system provides a clear margin of safety. The acceptance for $\pi^+\pi^-$ remains at the 95% level given this and even more stringent background suppression requirements.

6.1.4 Summary of Requirements

A dedicated PID system is required both for B-flavor tagging and to identify exclusive final states. These two purposes place different demands on the system: tagging requires positive identification of kaons and leptons with minimum pion background, mostly in the low-momentum range; measurement of exclusive decays requires positive tagging of pions with minimum kaon misidentification, mostly in the high-momentum range, resulting in the requirement of highly efficient π/K separation over the full spectrum.

These requirements also place constraints on the detectors and material located inside the PID system, in order to benefit fully from the intrinsic performance capability. Key issues include the accuracy of track extrapolation to the DIRC and a low level of backscattering and δ-ray backgrounds in the threshold ATC counter.

Likewise, the PID system must not significantly degrade the performance of the detectors located outside; both the physical volume occupied and material budget in radiation lengths are crucial in this respect. Of primary concern is the importance of calorimetry in measuring exclusive decays such as $B^0 \to \pi^0\pi^0$ and $B^0 \to \rho\pi$, for which gamma detection and mass resolution are essential.

6.2 Particle Identification Overview

To meet the requirements described above, a system containing two types of Cherenkov detectors has been incorporated into *BaBar*. The barrel region ($25.5° < \theta < 147°$) is covered by a DIRC [Rat92], which provides good performance over the whole momentum range while occupying only a thin radial region. An ATC covers the forward region ($17.1° < \theta < 23.6°$) augmenting the kaon tagging coverage and providing π/K separation up to $4.3\,\mathrm{GeV}/c$. The boundary between the systems was chosen to maximize the acceptance for particle identification within the constraints of magnet length and calorimeter position and angle. Both systems maintain low mass in order to minimize their effect on low-momentum photon calorimetry. The layout of the main components of the particle identification system is shown in Figure 6-2.

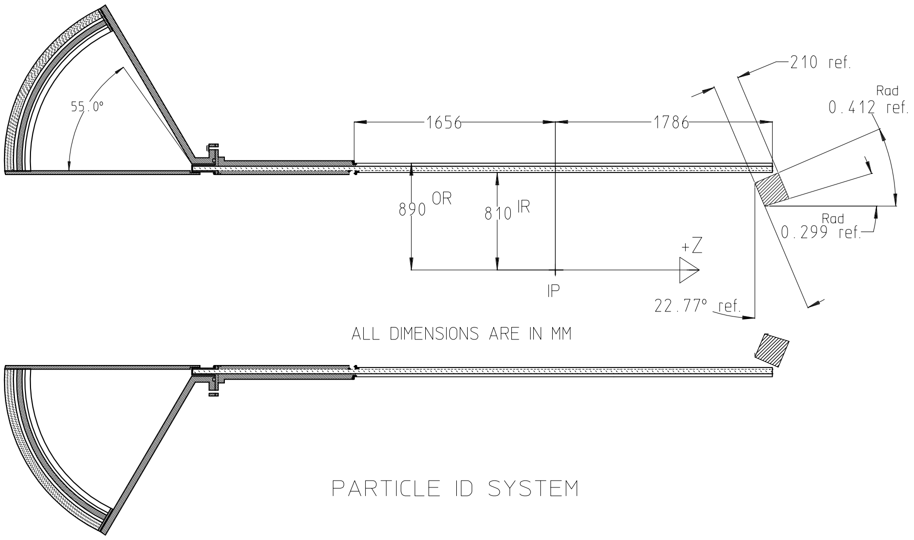

Figure 6-2. *Elevation view of the PID system geometry showing the barrel, DIRC, and forward ATC systems.*

6.2.1 The DIRC

A charged particle traversing a DIRC quartz bar with velocity β in a medium of refractive index n produces Cherenkov light if $n\beta \geq 1$. The DIRC Cherenkov radiators are 4.7 m-long rectangular quartz bars oriented parallel to the z axis of the detector. Through internal reflections, the Cherenkov light from the passage of a particle through the DIRC is carried to the ends of the bar as shown schematically in Figure 6-3. At the readout end, photons are detected outside the magnetic field region by conventional photomultiplier tubes (PMTs); a reflecting mirror at the other end of the bar returns forward-going light to the PMTs. For each track, the Cherenkov image expands from the end of the source bar across a standoff region filled with water to a toroidal surface of closely packed PMTs.

The DIRC uses as a radiator 156 quartz bars arranged in a 12-sided polygon around the beam line. This maximizes azimuthal coverage, simplifies construction, and minimizes edge effects. For sufficiently fast charged particles, some part of the Cherenkov radiation cone emitted by the particle ($\theta_c(E) = \cos^{-1}[1/\beta n]$, with $n = 1.474$) is captured by internal reflection in the bar and transmitted to the photon detector array located at the backward end of the detector. (Forward-going light is first reflected from a mirror located on the end of the bar.) The high optical quality of the quartz preserves the angle of the emitted Cherenkov light. The measurement of this angle, in conjunction with knowing the track angle and momentum from the drift chamber, allows a determination of the particle velocity. An advantage of the DIRC for an asymmetric collider is that the high momentum tracks are boosted forward,

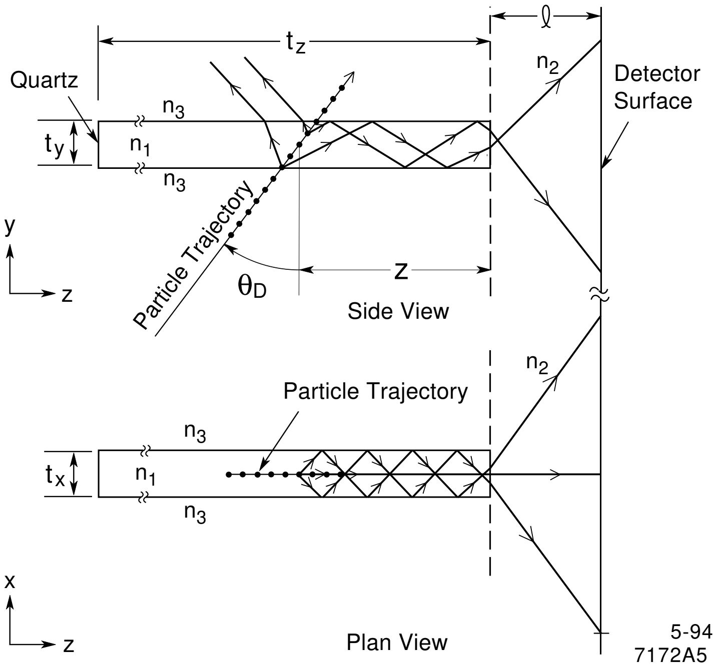

Figure 6-3. *Schematic of a single radiator bar of a DIRC counter. The particle trajectory is shown as a connected line of dots; representative trajectories of Cherenkov photons are shown by lines with arrows.*

which causes a much higher light yield than for particles at normal incidence. This is due to two effects: the longer path length in the quartz and a larger fraction of the produced light being internally reflected in the bar.

Each quartz bar is 1.75 cm thick, 3.5 cm wide, and 470 cm long, and is constructed by gluing together four shorter bars. The total radial thickness of the DIRC, including quartz thickness, sagitta from the polygonal shape, mechanical supports, and a 1 cm clearance on each side, is 10 cm. This material represents $0.18X_0$ at normal incidence. An effort has been made to minimize both the radial thickness and the amount of material, since these increase the radius and cost of the barrel calorimeter while degrading its performance for soft photons.

The photon detector consists of 13,400 conventional 1.125-inch-diameter phototubes. They are organized in a close-packed array at a distance of 120 cm from the end of the radiator bars. The phototubes, together with modular bases, are located in a gas-tight volume as protection against helium leaks from the drift chamber.

The photo-detection surface approximates a partial cylindrical section in elevation and a toroid when viewed from the end. The standoff region has reflecting surfaces along the inner and outer radii to reduce the number of phototubes required. The opening angle between these surfaces is still under review but is taken to be 55° at this time. To maintain good photon transmission for all track dip angles, the standoff region is filled with water. The water seal occurs at a quartz window that is glued to the end of the bar assemblies. Most of the mass of the standoff box structure is high permeability steel, which provides adequate magnetic shielding for the phototubes.

The DIRC radiators are supported on the central support cylinder, which is cantilevered from the strong support tube. Alternative designs that do not require a cantilevered support for the central support cylinder are also under consideration. Both the strong support tube and the standoff box are supported by a yoke directly to the barrel IFR. Since the DIRC bars penetrate the backward endcap return iron, the DIRC mechanical design interacts strongly with other structures at the backward end of the detector (Section 6.4.1).

A single-bar DIRC using 47 phototubes with an air standoff has demonstrated this detector concept (Section 6.4.5). A larger prototype with a realistic water standoff region will shortly be tested in a particle beam. It will be capable of imaging almost all Cherenkov patterns on a track-by-track basis. This prototype and other laboratory measurements will provide a detailed test of the optical quality of the quartz, glue joint, and mirrored surfaces, and establish the performance (single photoelectron response, quantum efficiency, and timing resolution) using approximately 500 PMTs. The prototype will also be used to test front-end electronics.

6.2.2 The ATC

The forward PID detector is a silica aerogel Cherenkov counter covering the polar angle range $17.1° < \theta < 23.6°$. Both kaon tagging and pion identification are achieved with two refractive indices, $n \simeq 1.0065$ and $n \simeq 1.055$.

There are two key components in the ATC system: the aerogel radiator and the readout device. Candidates for both are commercially available from well-established suppliers. Several suppliers of aerogel with a polymer gel structure have been identified; material with the appropriate density range, transmittance, purity, and anticipated stability has been obtained in small quantities.

Aerogel with good optical quality is produced by Airglass, Lockheed, Jet Propulsion Laboratory (JPL), Lawrence Livermore National Laboratory (LLNL), Aerojet, and the Budker Institute of Nuclear Physics (BINP) at Novosibirsk. Caltech's Space Radiation Laboratory regularly uses large aerogel blocks from Airglass in balloon-based Cherenkov detectors. Lockheed's production facility can, in principle, produce enough high quality aerogel for our needs in 10 months [Men94]. The aerogel produced by JPL is hydrophobic, has good optical transmittance [Tso94], and has been extensively tested in our beam measurements. A two-step process for aerogel production has been developed by LLNL and is being transferred to the commercial company Aerojet [Hru94].

In order to collect Cherenkov photons efficiently inside the solenoid, the photon detector must work in magnetic fields up to 1.5 T, have a large UV-sensitive area with high quantum efficiency, and have low noise. The baseline design uses bialkali fine mesh photomultiplier tubes (FM PMT) from Hamamatsu with a newly developed high quantum efficiency photocathode. Hamamatsu's FM PMTs with conventional bialkali photocathodes have been widely used in high-energy experiments [Gil88] for many years.

The average thickness in front of the endcap calorimeter is 9.5% of a radiation length. However, the present design places phototubes in the active region in front of the DIRC. The implications of this for DIRC and calorimeter performance need further study.

6.3 Projected Performance

6.3.1 Simulation Based on Prototype Results

The barrel DIRC and forward aerogel detectors are being studied using the simulation programs ASLUND and BBSIM. The former, based on fast parameterizations of the detector responses, allows studies requiring high statistics, and the GEANT-based BBSIM program provides a tool for simulating whole events more realistically. In the latter, other subdetectors in *BaBar* are defined with materials and geometries consistent with their present designs. This provides a fairly realistic source for secondary processes representing event-related backgrounds. Primaries are tracked as well as the secondary products they produce, such as δ-rays, pair production, hadron scattering, backsplash, and decays. PID detector geometries are defined to a high level of detail, and simulation of response is tuned to the prototype test results (Section 6.4.5).

Barrel DIRC Detector

ASLUND Simulation. The behavior of the DIRC has been simulated in the ASLUND program; much of it is calculated analytically, and part is done approximately. The parameters for some of the approximations are adjusted to agree with the results of a stand-alone simulation of the DIRC. This program includes the propagation of photons to phototubes placed on a toroidal detector surface and the calculation of errors in the measured angles; it accounts for absorption in the quartz, in the water, and at surfaces; it calculates the π/K

separation taking into account all ambiguities. Some aspects, such as the 12-sided geometry and the wavelength dependence of the absorption, are done in an approximate way. This simulation ignores background effects from δ-rays and other tracks, so its estimates are somewhat optimistic. In the future, GEANT simulations that include background effects will be used to determine the parameters used in the ASLUND simulation.

BBSIM Simulation. The barrel DIRC has been implemented in BBSIM with a realistic geometry. The detector description is parameterized in an easily modifiable form to create a description of the detector close to the engineering drawings. The active length of 178.6 cm in the forward direction provides an angular coverage to $\cos\theta = 0.91$, and 2 cm gaps between the modules result in a 4% loss in azimuth. The radiator represents $0.18X_0$ at normal incidence. All physics parameters, such as absorption lengths, refractive indices, and overall photoelectron yield, are tuned to the prototype test results.

The generation and propagation of Cherenkov photons are fully simulated. After tracking is complete, all particles crossing the DIRC with momenta above Cherenkov threshold are processed through a customized simulation. Photons are generated with a Poisson distribution along the curving track trajectory through the radiator. Dependence of the refractive index $n(E)$ of the radiator on photon energy is used to generate photons emitted at the Cherenkov angle $\theta_c(E)$. Photons produced in the DIRC bars are propagated until they reach the phototube detector surface. Light transport includes total internal reflection inside the quartz bars, diffraction at the quartz/water interface, and possible reflections from the mirrors at the forward end of the bar or within the standoff tank. Losses due to absorption in the bars or the water are included as functions of the photon energy. Photon absorption at the mirrors, scattering by surface imperfections, reflection of light at the quartz-water boundary (including the effects of photon polarization and angle of incidence), and the quantum efficiency of the PMT photocathode are also taken into account. Photons which strike the sensitive area of a PMT are recorded with digitized spatial and time information. A typical event with one B decaying to an arbitrary channel and the second B to $\pi^+\pi^-$ has been projected onto the phototube detector plane in Figure 6-4(a). The time window for background in the simulation is 15 ns. Four charged tracks reach the DIRC: $\pi(4.1)$, $\pi(2.1)$, $K(0.61)$, and $\pi(0.25)$; the momenta, in GeV/c, are indicated in parentheses.

Measurements made in cosmic ray Prototype-I tests (Section 6.4.5) have been used to tune the absorption coefficients and the reflection efficiencies at the bar surfaces and mirrors. The resulting comparison between predicted and measured numbers of photoelectrons at various positions and angles are in excellent agreement, as illustrated in Figure 6-5.

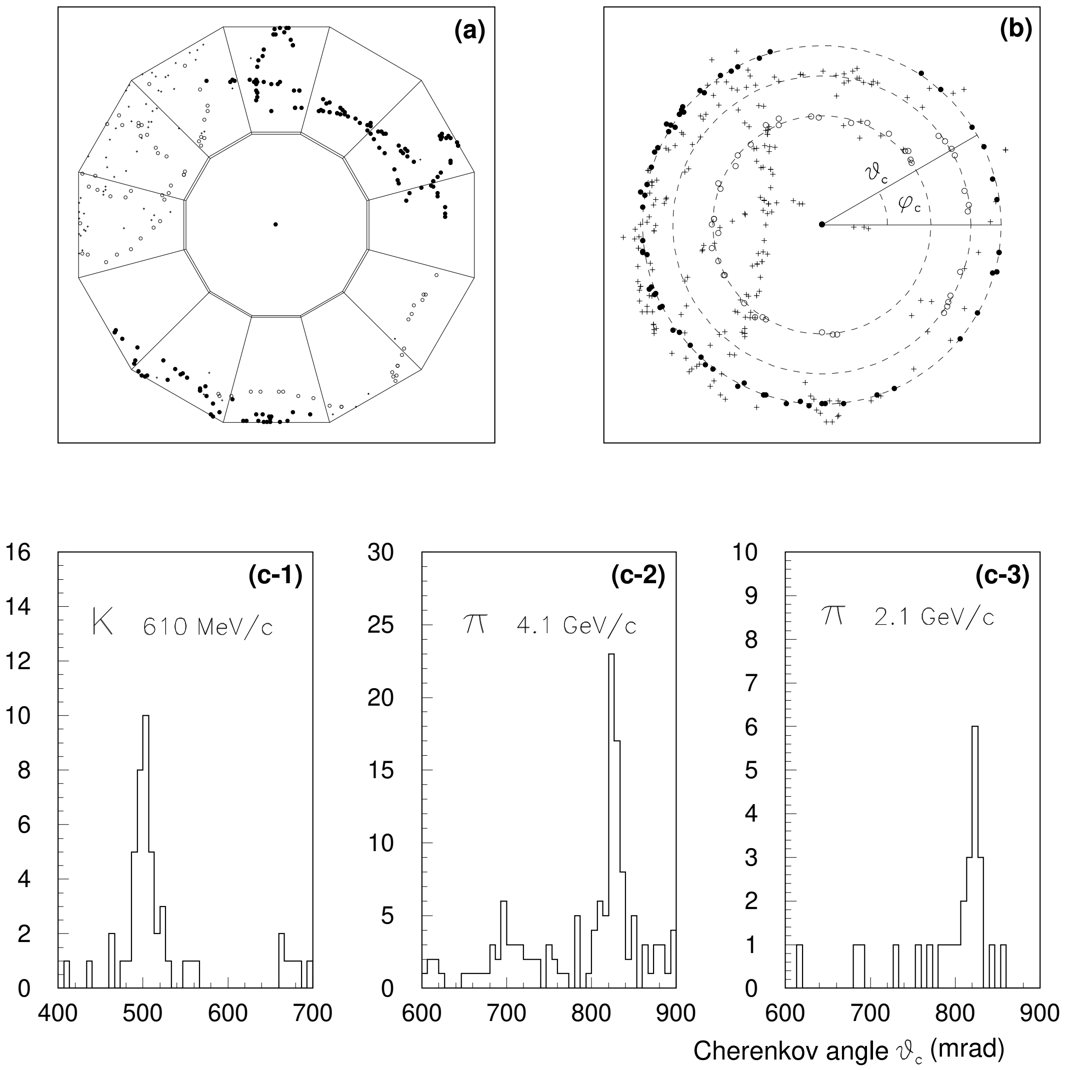

Figure 6-4. *(a) PMT hits projected onto the x-y plane. The particles producing the hits have distinctive markers: Cherenkov images (conic sections) from the $B \rightarrow \pi^+\pi^-$ decays are shown as solid circles, hits from the two other charged tracks as open circles, and from the secondary tracks as '+'. (b) PMT hits projected in Cherenkov angle space with the four tracks superimposed at the center. The hits from the two pions from the B decay overlap at the largest radius, $\phi_c \approx 820\,\mathrm{mr}$. The '+' marker in this case corresponds to assignment ambiguities. (c) Cherenkov angle projections for three of the tracks and the associated ambiguities.*

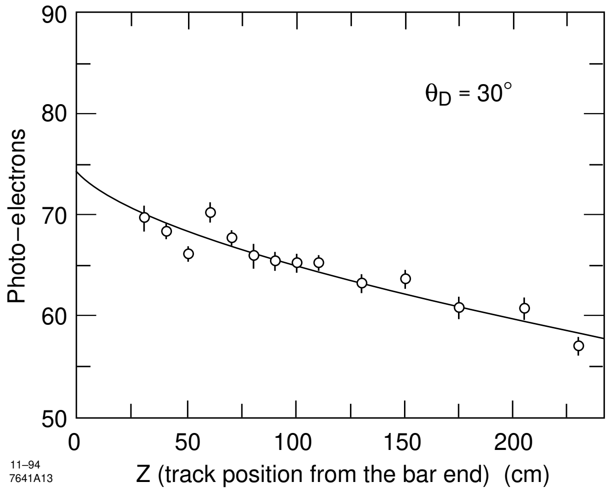

Figure 6-5. *Simulated photon yield (solid curve) compared to track position dependence of the photoelectron yield at a dip angle of $\theta_D = 30°$ as measured (circles) in Prototype-I using cosmic rays.*

Forward Aerogel Detector

The forward aerogel PID simulation in ASLUND is based on test beam results and the measured single photoelectron response of a FM PMT. The photoelectron yield of the phototube is described by a Poisson distribution with an excess noise factor of 2. The mean of the distribution is determined by the length of the trajectory through the aerogel block, where the full length at normal incidence corresponds to 10 photoelectrons. The output of the simulation is the pulse height in photoelectrons reflecting the single photoelectron pulse-height distribution of the FM PMT.

A simulation of the forward PID system has been developed in BBSIM. The geometrical description will correspond to the present design of the ATC with two layers and include a realistic simulation of the mechanical structure fabricated in carbon or fiberglass, as well as two rings of FM PMTs located on the inside and outside of the two aerogel layers. The geometry is fully parameterized for easy testing of options.

6.3.2 Pattern Recognition in the DIRC

The complex event of Figure 6-4(a) illustrates that the Cartesian coordinates of the hits are not the easiest representation with which to do pattern recognition, *i.e.,* to assign hits to tracks. The most appropriate change of variable appears to be from Cartesian coordinates to Cherenkov angle θ_c. In the representation in which the track segment defines origin and dip angle, the matching hits cluster at the radius corresponding to the particle species. This not only leads directly to a measurement of Cherenkov angle, but also obviates the need for sophisticated pattern recognition (see Figure 6-4(c)).

Cherenkov Angle Measurement and Mass Hypothesis Testing. Photons are presumed to originate from the centers of curved track segments. They are seen by a PMT as an image on the far side of the plane interface between the standoff tank and the quartz bar. A ray can be traced back from the PMT to the center of the quartz bar with a single refraction at the quartz-water interface. The angle between this ray and the track segment is the measured value of θ_c. The azimuthal angle ϕ_c is also determined in this manner. The optical distance (corrected for refractive index) from track to PMT is used to estimate the arrival time of the PMT signal.

Up to a 16-fold ambiguity exists in the determination of θ_c because the number of bounces off the quartz walls and the mirrors is unknown. Only one solution is correct in each case, provided the photon is truly associated with the given track. Ambiguities can be eliminated when the corresponding photon path yields unphysical values for reflection, refraction, or Cherenkov emission angle. Timing information will also be used to reject solutions when the computed and measured time of arrival for a photon at the PMT are inconsistent. On average, only two solutions remain with a timing cut of $\pm 7.5\,\mathrm{ns}$. Tighter timing cuts may be available, depending on the choice of phototube and readout system.

For each track, the distribution of the Cherenkov angles of all potentially associated photons shows a clear peak, corresponding to the parent particle type, above a background of wrong track-hit associations (Figure 6-4(c)). The peak position and the number of photoelectrons are then compared to that expected for each particle type and a mass assignment made on the basis of an hypothesis test. Consistency between angles and timing information will also be checked using the expected relationship between θ_c and ϕ_c for a hit and the propagation time for the photon to reach the PMT (Figure 6-6).

Intrinsic Resolution. The full DIRC pattern recognition algorithm has been applied to single pion samples to estimate the intrinsic resolution of the Cherenkov angle θ_c. The single photoelectron θ_c resolutions are approximately 9.5 mr, largely independent of track momentum and dip angle. The number of associated photoelectrons per track is given in Table 6-1. In this study, the availability of precise timing information was not taken into account. The intrinsic resolution of the DIRC detector is obtained assuming that the N_{PE} individual measurements of θ_c are uncorrelated.

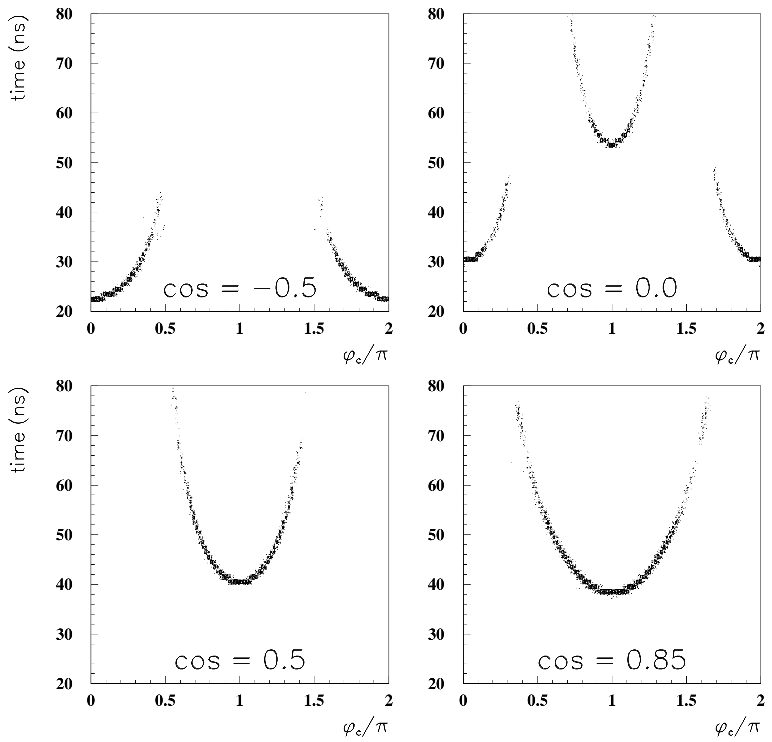

Figure 6-6. *Measured time at the PMT face as a function of the photon Cherenkov azimuthal angle ϕ_c for several track polar angles. The track momentum is 4 GeV/c, and the value $\varphi_c = \pi$ is defined for a photon whose initial direction projected onto the bar plane is towards the mirror.*

Momentum	Sine of Particle Dip Angle			
(GeV/c)	–0.5	0	0.5	0.85
0.500	39	22	25	—
0.800	34	31	28	61
1.000	36	35	29	58
2.000	39	38	31	61
4.000	41	41	32	60

Table 6-1. *Mean value of the number of detected associated photoelectrons as a function of pion momentum and sine of the dip angle. The effective packing fraction, i.e., the ratio of active to total surface, is assumed to be 53% for this estimate.*

Momentum	Sine of Particle Dip Angle			
(GeV/c)	-0.5	0	0.5	0.85
0.500	7.1	2.9	7.0	—
0.800	4.7	2.6	5.1	4.6
1.000	4.0	2.5	4.2	4.4
2.000	2.8	2.2	2.9	2.7
4.000	2.2	2.1	2.4	2.0

Table 6-2. *Resolution on the θ_c (mr) measurement per pion from* BBSIM. *Charged tracks are extrapolated from the vertex to the DIRC bars.*

Effective Resolution. The DIRC performance is not dependent on intrinsic qualities alone. At low momentum, the resolution of the Cherenkov angle measurement is mainly determined by resolution of the track extrapolation, in addition to multiple scattering in the DIRC itself.

Using the reconstruction algorithm which is currently available in BBSIM, track parameters are obtained at the point of closest approach to the IP by a progressive fitting procedure using drift chamber and silicon vertex detector hits. Therefore, the procedure for swimming the track from the primary vertex to the DIRC includes angular errors coming from Coulomb scattering in the support tube and the inner wall of the drift chamber. As a result, the angular errors at the DIRC are significantly overestimated by BBSIM, especially in azimuth. Table 6-2 gives the resulting effective θ_c resolution per track. A procedure with better accuracy would be to use a Kalman filter fit to extrapolate track parameters from the outer drift chamber layers to the DIRC. Track extrapolation errors would then include only the effect of the material between the last drift chamber hit and the quartz bar, which is equivalent to $0.02X_0$ at normal incidence. From preliminary results, the quoted errors on the extrapolated angle should be reduced by 10 to 40% using such a technique. A constrained fit to the Cherenkov image may further improve upon the errors.

6.3.3 Particle Identification in the DIRC

The ultimate performance of the DIRC is limited by the Cherenkov angle difference between particle species. In a quartz radiator (with $n = 1.474$), the difference in Cherenkov angle between a pion and a kaon is fairly large at low momenta but is as small as 6.5 mr at 4 GeV/c. The same difference occurs between a muon and a pion at 770 MeV/c.

Figure 6-7 shows the K/π separation as a function of track momentum and $\cos\theta$, obtained with the ASLUND simulation of DIRC performance. The separation is very clear in the

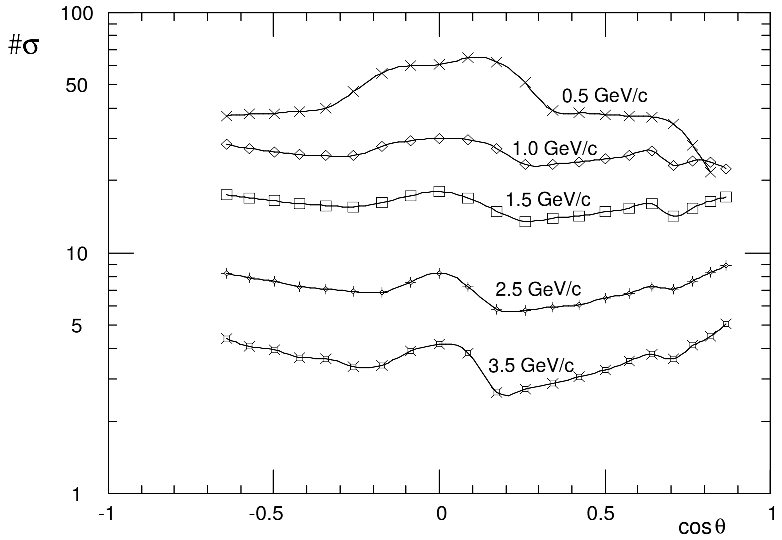

Figure 6-7. *Predicted K/π separation performance of the DIRC, quoted in terms of the number of standard deviations, vs.* $\cos\theta$*, for different momenta.*

momentum region that is most interesting for tagging kaons in the barrel, 0.5 to 1.5 GeV/c, which is why the kaon tagging efficiency is so close to the ideal case. The separation is always $\gtrsim 4\sigma$ for particles within the kinematic limits for B decays, as can be seen in Figure 2-13.

Table 6-3 shows similar information on π/K separation, but for both ASLUND and BBSIM simulations of single track samples. This comparison is meant to illustrate the range of performance estimates obtained from current simulations. The ASLUND results in column (a) are known to be somewhat optimistic due to a lack of background, but on the other hand do not incorporate potential improvements brought about by a constrained fit to the Cherenkov image. The BBSIM results in column (b) include the effects from a realistic simulation of background hits but overestimate the contribution due to the track angle uncertainty because of the extrapolation of errors from the vertex and also do not incorporate a constrained fit. The actual π/K separation is probably somewhat better than the ASLUND result, but the comparison between the two simulations is an instructive measure of the reliability of predictions from our present understanding. It is clear that good π/K separation is achievable in most of the phase space of the asymmetric collider.

BBSIM as well as ASLUND studies show that a μ/π separation with greater than 2σ can be achieved by the DIRC at momenta below about 500 MeV/c. The separation power is somewhat spoiled by the track direction uncertainty due to multiple scattering. However, a separation of more than two standard deviations up to 500 MeV/c may be of great interest for tagging purposes and is likely to improve with more accurate track fits and extrapolations.

Momentum GeV/c	Sine of Particle Dip Angle							
	-0.5		0		0.5		0.85	
	a	b	a	b	a	b	a	b
0.500	38	68	60	167	38	69	—	—
0.800	35	35	40	63	33	32	24	36
1.000	27	26	30	42	25	25	23	24
2.000	11.0*	9.3*	12.2	11.7	9.7	8.9	9.7	9.6
4.000	2.9*	3.0*	3.1*	3.0*	2.3*	2.7*	3.9	3.3

Table 6-3. *π/K separation in standard deviations as a function of track momentum and the sine of the dip angle from a simulation using (a)* ASLUND *and (b)* BBSIM. *The $*$ entries are outside the kinematic region populated by B decays.*

6.3.4 Particle Identification in the ATC

Projected particle identification capabilities of the aerogel system are based on beam tests. The $n = 1.0085$ aerogel counter's response to 3.5 GeV/c positive pions and protons (below Cherenkov threshold) was measured (Figure 6-8). If a cut is made at 55 ADC counts, corresponding to 1.5 photoelectrons, one obtains a 97% efficiency for pion detection with a 3% misidentification of below threshold particles. Similar separation between pion and kaons was also obtained at 3.5 GeV/c after subtraction of the background due to electronic noise, wrongly tagged pions, and kaon decays.

For the current design, the Monte Carlo simulation tuned with our test beam results shows that a β=1 charged particle passing through the aerogel produces a signal of more than ten photoelectrons in both the low and high refraction index aerogel blocks. With a ten photoelectron signal, the aerogel PID system will give π/K separation up to $\simeq$ 4.3 GeV/c [Oya94], as shown in Figure 6-8.

6.3.5 Performance Requirements for Track Reconstruction

In a simple model, the measurement error of the Cherenkov angle per track in the DIRC can be written

$$\sigma_{\theta_c}^2 = \left(\frac{\sigma_{PE}}{\sqrt{N_{PE}}}\right)^2 + \sigma_{trk}^2 + \sigma_{ext}^2,$$

where $\sigma_{PE}/\sqrt{N_{PE}}$ is the intrinsic resolution, σ_{trk}^2 is the track angular error at the last drift chamber layer, and σ_{ext}^2 is error on extrapolation to the DIRC due to multiple scattering in the outer wall of the drift chamber and in the DIRC supports. The study of errors due

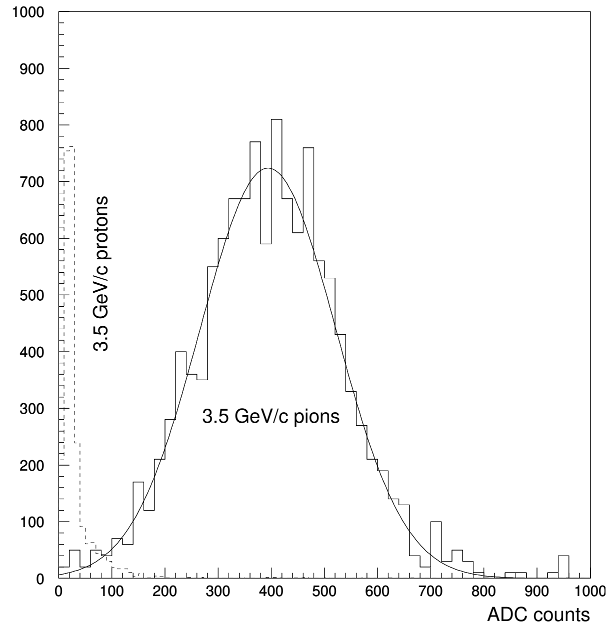

Figure 6-8. *Responses of a prototype 1.0085 aerogel counter to 3.5 GeV/c pions (solid line) and to the below threshold protons (dashed line) in a 1.3 T magnetic field.*

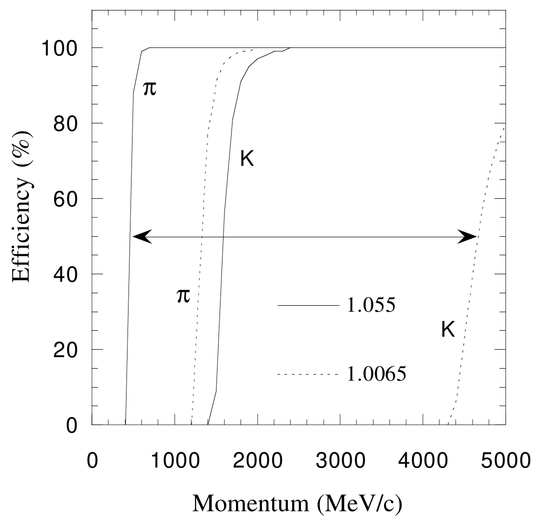

Figure 6-9. *Threshold curve for pions and kaons as a function of momentum for a two-index aerogel system.*

to multiple scattering in the quartz bar itself, which contribute to σ_{PE} but are not fully uncorrelated, requires further work. In principle, these effects can be reduced by fitting the Cherenkov image.

Clearly, it would be desirable to maintain the track error contributions, due to the resolutions on the projected angles θ and ϕ, below the intrinsic resolution (*i.e.,* below 1.0 mr) at least for large momenta at which the π/K Cherenkov angle difference is small. In this context, it is important to minimize the amount of material between the drift chamber and the DIRC radiator. For example, increasing the amount of material to 8% of a radiation length at a 60° dip angle (*i.e.,* twice the present design) would lead to more than 1 mr uncertainty for a 4 GeV/c track due to multiple scattering. The present design of the drift chamber and DIRC support achieves this goal, as shown in Figure 5-5.

Background Source	Primary Track-Equivalent/Event
Event-Related Background	4.7
Beam-Gas EM (10×nom.bkg)	0.60
Radiative Bhabha	0.11
PMT Noise	0.020
Cosmic Rays	0.00016
Others	Negligible

Table 6-4. *Backgrounds in primary track-equivalent units (33 photoelectrons per track) for a readout time of 50 ns.*

6.3.6 Effects of Backgrounds on PID Detector Performance

Effects of Backgrounds on DIRC Response

Several background sources can affect the performance of the DIRC, such as event-related backgrounds, synchrotron radiation photons, beam-gas interactions, cosmic rays, phototube dark current BBSIM has been used to simulate the detector response. Each random background source has been integrated over an assumed 50 ns readout time, and the probability of a double hit in the same PMT in one event has been studied for readout times of 50 ns and 100 ns.

Event Related Backgrounds. Based on a BBSIM simulation, a typical $\Upsilon(4S) \rightarrow B^0\overline{B}^0$ event produces an average of 345 photoelectrons detected in the DIRC. Of these, 190 are attributed to an average of 5.7 primary tracks which lie within the DIRC acceptance and have momenta above Cherenkov threshold. Thus, each primary particle contributes 33 photoelectrons. The other hits are due to secondary tracks produced in the detector, mostly in the form of backsplash from the electromagnetic calorimeter, that have much softer momentum spectra than the primary tracks. Their random angular distribution gives an event-related background in the DIRC, which manifests itself in the angular coordinate system used for pattern recognition as a flat contribution under the Cherenkov peaks for primary particles. This background can be subtracted easily.

Other Backgrounds. The machine is a source of backgrounds from lost particles, radiative Bhabhas, and other backgrounds as discussed in Chapter 12. The largest source of machine-related background is the beam-gas electromagnetic term as shown in Table 6-4. Other backgrounds such as synchrotron radiation, cosmic rays, and PMT dark current have very small or negligible impact on the DIRC response.

Multihit Probability. On average, 175 PMTs are hit by the 190 photons associated with measurable tracks in a *BaBar* event, giving a double-hit probability of $\sim$8%. Including hits due to event-related background, the number of PMTs with a double hit increases to 16 and the probability becomes 9%. If beam-gas interactions are included at 10 times nominal background, the double-hit probability is 9.2% for a read-out time of 50 ns and 9.5% for a readout time of 100 ns.

Effects of Backgrounds on ATC Response

Since each cell is read out by a PMT placed outside the Cherenkov radiator, charged particles passing through a PMT pose little problem for particle identification in the ATC. One background source is shower leakage from the calorimeter. For incident photons, this is generally not a problem, as no track will point to that cell; one can actually use the photons to determine the size of the effect. Backsplash from electromagnetic showers consists mostly of photons and electrons below Cherenkov threshold. The photons cause a problem only to the extent that they convert in the material of the PID system.

Another background is δ-ray production, since a below-threshold kaon can be misidentified as a pion by knocking out an electron with momentum above Cherenkov threshold. Both an analytic calculation [Oya94, Gro92] and a detailed GEANT simulation [Shi94] have been used to study the effect. The results are in good agreement with measurements in beam tests. In the forward direction, the study shows that $\sim$1% of 4 GeV/c kaons may be misidentified as pions due to δ-ray production in the drift chamber wall and backsplash from the calorimeter. With $\sim$97% detection efficiency for pions, the system still provides $\sim 4\sigma$ π/K separation at 4 GeV/c. Though δ-ray production and backsplash cause about a 2–3% probability of misidentifying a low momentum ($p < 1.2$ GeV/c) kaon as a pion, they do not affect $B \to \pi\pi$ and $B \to \pi K$ separation since both daughters from these decays have $p > 1.5$ GeV/c. In the worst case, such $K \to \pi$ misidentification results in a B tagging inefficiency of less than 3%.

Synchrotron radiation photons are not expected to cause problems. Their energies lie between 4 and 100 keV, and cannot produce any above threshold (1 MeV for $n = 1.06$) electrons. Their wavelengths are also not in the photocathode-sensitive region.

Beam-gas background should not be a problem either with a 100 ns integration time (the PMT's pulse width is a few tens of ns). The average number of hits per microsecond in the whole CsI calorimeter is about 0.8. Therefore, fewer than 0.08 hits per 100 ns are expected over the 144 aerogel cells, corresponding to ≤ 0.0005 hits per cell during one readout cycle.

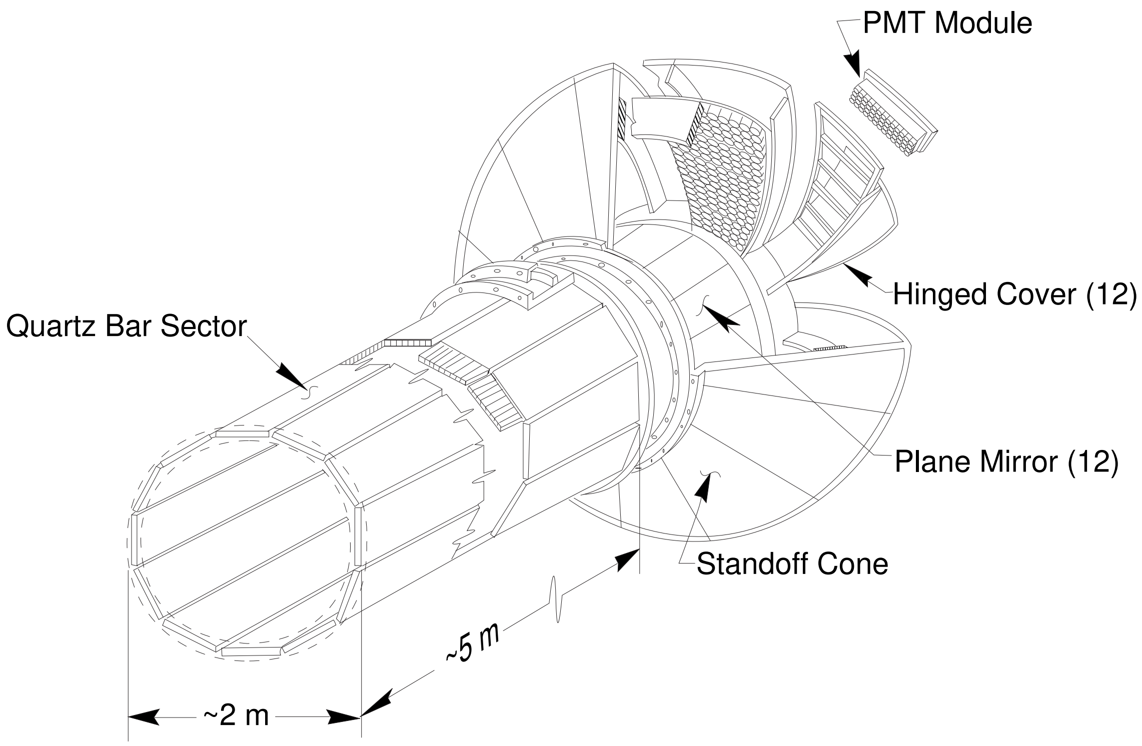

Figure 6-10. *Mechanical elements of the DIRC.*

6.4 The DIRC Detector

6.4.1 DIRC Mechanical Design

Principles of Operation

The major mechanical elements of the DIRC, shown schematically in Figures 6-10 and 6-11, include the following.

Quartz Radiator Bars and Sectors. The bars must have small attenuation loss for $\lambda \geq 300\,\mathrm{nm}$. The surfaces must be accurately rectilinear and smooth to preserve light angle and intensity after many reflections. The choice of bar thickness and width involves trade-offs among light intensity, angular resolution, material ahead of the calorimeter, and cost. The bars are assembled into 12 separately covered and mounted sectors of 13 bars each. The bars of a sector are united at the water boundary by a glued quartz window which is sealed by an O-ring to the assembly flange.

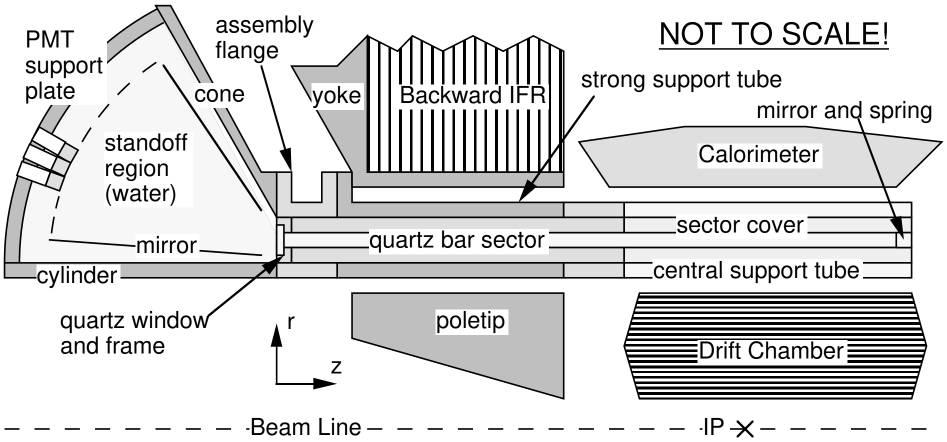

Figure 6-11. *Schematic of the DIRC support system.*

Support Tubes and Assembly Flange. The central support tube is an aluminum honeycomb between cylindrical skins which holds the sectors within the sensitive volume of the detector. Its material thickness in radiation lengths will be small compared to the quartz bars. The central support tube will be cantilevered from the strong support tube. This steel tube, axially aligned with the central support tube, also holds the quartz sectors. It is mounted inside the backward IFR and is the central structural element of the DIRC, strong enough to support the beam line elements and the backward poletip. The steel tube is supported independently by the barrel IFR. The assembly flange is a short aluminum section rigidly connecting the strong support tube to the standoff region. Its functions are to reduce the magnetic flux coupled to the PMTs, to seal the sector windows, and to support and seal the inner and outer radius boundaries of the standoff volume.

Standoff Region and Mirrors. A water-filled volume between the windows at the ends of the quartz sectors and the PMTs permits the Cherenkov image to expand. The volume is defined by a cylindrical inner boundary and a conical outer boundary that nearly meet at the sector windows, plus a back toroidal surface covered by the PMTs. The walls are of high-quality magnetic steel to eliminate the effects of stray magnetic fields on the PMTs. Pure water is inexpensive, gives plenty of light transmission, and matches quartz fairly well in index of refraction and dispersion. There are 24 flat mirrors azimuthally aligned with the sectors. Half are mounted on the inner radius cylinder, the others on the cone at a 55° angle to the beam line. The choice of this angle is a compromise between the number of PMTs needed and ambiguities in the Cherenkov images and is still under review. To minimize mirror distortion from stress, a neutrally buoyant honeycomb structure is proposed.

Phototubes. The PMTs need good single photoelectron response and good quantum efficiency for $\lambda \geq 300\,\mathrm{nm}$. The PMT faces are immersed directly in water, covering the entire back toroidal surface in a close-packed geometry. The module geometry for the PMTs has not been finalized. If individual tubes (or very small modules) are used, the toroidal steel PMT support plate (Figure 6-12), located at a radius somewhat larger than that of the PMTs, can accommodate the necessary access holes without sacrificing either mechanical structure or magnetic shielding at the PMT face. Steel cover plates that would limit access will be avoided.

Quartz

The quartz bars will be made from bulk natural fused quartz (*e.g.,* VITREOSIL 055). This material has an index of refraction of 1.474, good light transmission for $\lambda \geq 300\,\mathrm{nm}$, is reasonably radiation hard, and is relatively free of bubbles and inclusions. This bulk material will be used to produce bar pieces of $117.5 \times 3.5 \times 1.75\,\mathrm{cm}^3$, which will be glued to form 156 full-length bars. These dimensions were chosen with cost, photoelectron yield, angular resolution, and minimization of material in front of the calorimeter in mind. The bars need to be extremely rectilinear to preserve the Cherenkov image, and well polished to preserve the light after many reflections. We have set up an optical laboratory for quality control and characterization of all the optical properties of the quartz bars. Cosmic ray tests, as described in Section 6.4.5, indicate that commercially produced bars meet the requirements.

The decision to glue short bars together to form a full-length radiator is driven by the excessive cost of tooling needed to cut and polish longer bars at standard optical industry shops. An epoxy with excellent optical properties and sufficient mechanical strength to join the short bars together has been selected and tested. Alignment fixtures and gluing jigs will be used in the process. Radiation hardness of the quartz, the epoxy, and its long term properties will be verified. Since the bars are read out in one direction, mirrors will be needed on the other end. We will use glass mirrors coated on the front surface with aluminum and silicon dioxide. For maximum reflection, the mirror will not be coupled optically to the bar end since many photons are internally reflected.

Sectors and Covers

There are several reasons that the quartz bars are arranged in azimuthal subassemblies or sectors. First, for structural reasons, it is necessary to allow azimuthal gaps for ribs to couple the inside and outside radii of the DIRC support tubes. Second, a water-tight seal is needed at the junction with the standoff region. Third, the optics of the standoff region work best to maintain the resolution and minimize reconstruction ambiguities if the mirrors are flat and aligned with the sectors. These conditions tend to drive the sector multiplicity down.

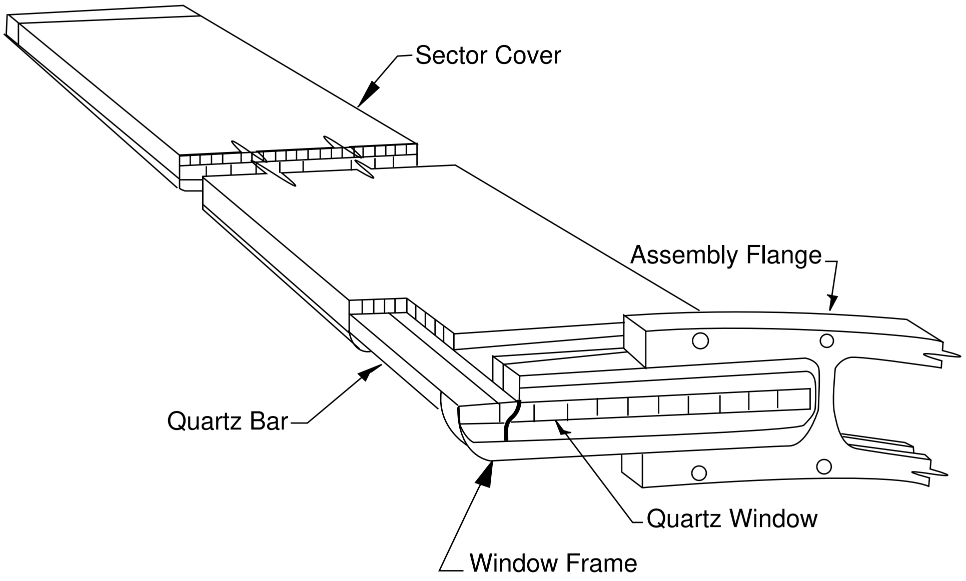

Figure 6-12. *Schematic view of bars assembled into a mechanical and optical sector.*

On the other hand, they increase the radial width of the DIRC, not only because the sagitta is proportional to the square of the sector width, but also because the stiffness of the sector covers is a sensitive function of the width. For the parameters considered here, the radial budget is: sagitta, 3 cm; quartz and gaps, 2 cm; sector covers, 2 cm; and support tubes, 1 cm; for a total of 8 cm. The minimal azimuthal gap, between the inside corners of quartz bars in neighboring sectors, is 1 cm, which is sufficient to accommodate side-by-side O-rings. The average coverage loss between sectors is then approximately 2 cm, less than 5% of the total circumference.

The bars are assembled into a mechanical and optical unit or sector on a long optical table. At the end near the standoff region, each bar is glued to a common 3 mm-thick quartz window. The window area is somewhat larger than that of the bars so that light can emerge unimpeded at large angles from all parts of the sector. Because the bars are close together with sides parallel, care must be taken to avoid optical crosstalk. For this reason, the bars are separated at the support points by thin, small-area plastic wafers aluminized on both sides. To seal the sector at the standoff region, an aluminum window frame is sealed by O-rings; first to the back of the window and then to the assembly flange as the final part of sector installation. Some details are shown schematically in Figure 6-12.

In our present design, each bar is supported at 0.6 m intervals, 0.3 m from the glue joints. In this geometry, each joint is normally at a point of maximal (but very small) stress, but it is subjected to zero additional stress due to a misalignment of one of the nearest supports.

For the part of the sector inside the sensitive region of the detector, ~3 m in length, the periodic bar supports are mounted to top and bottom plates of low density honeycomb, 1 cm thick by 42 cm wide, which are coupled together by thin strips on the sides. The periodic supports are strengthened by a transverse stiffener, which is a few centimeters wide axially. The bars do not touch the honeycomb or its stiffeners directly but are spaced below by an aluminized 1 mm-diameter fiber and clamped on top by a threaded screw, aluminized on the tip. Transverse support is supplied by stressing the spaced coupling strips on the sides, so that the cover supports the sector independent of orientation. The part of the sector outside the sensitive region of the detector, ~2 m in length, has top and bottom cover plates of solid aluminum.

To protect the glue joints during extreme (*e.g.,* seismic) axial motion, each bar is compressed at its own weight ($<$ 100 kg/sector) by spring loading the front surface mirror at the non-readout end of each sector. The force is returned to the window by the tension in the thin skin (0.1 mm stainless steel) outer layer of the sector cover. Because the covered sectors can easily be made gas tight, the internal atmosphere is readily controlled by a nitrogen purge.

Support Tubes and Assembly Flange

Figures 6-10 and 6-11 illustrate the concepts discussed in this section. Very different structures are needed to support the sectors in the sensitive (central support tube) and insensitive (strong support tube) parts of the detector.

The central support tube must be as thin as feasible. The problem is made somewhat difficult by the long distance from the major structural elements of the DIRC. To avoid coupling this relatively fragile assembly simultaneously to structurally independent ends of the detector, one of the proposed designs uses a cantilever. The major structural elements are aluminum: 1 mm-thick skins at inner and outer radii; 3 mm-thick circumferential ribs slotted for the sectors and spaced every 0.6 m; and 2 mm-thick axial ribs every 30° linking the circumferential ribs. The average material thickness of the support tube is $\leq 0.04X_0$. Carbon-fiber support structures will be studied in order to further reduce the radiation-length thickness. Studies using a finite element analysis show that this design will carry the required load of 17 kg per meter per sector. The structure is predicted to deflect a few millimeters when loaded, with buckling the nearest failure mode. The load limit can be increased by distributing the forces at the corners of the ribs. Inside the central region, but beyond the maximum angle of the barrel calorimeter, the central support tube is a heavy aluminum structure like the steel strong support tube to which it is joined. This design reduces the required length of the low density cantilever.

The strong support tube, located inside the IFR, requires steel for strength and for returning magnetic flux from the poletip. To accommodate whatever solution is adopted for beam line support, the strong support tube is designed to support, in addition to the DIRC, the backward beam line elements and the poletip, which feels an axial force of 300 tons at 1.5 T. Given septa of 1 cm width every 30° to couple the inner and outer skins, careful analysis shows that the tube is strong enough for this worst case. Unlike the central support tube, the strong support tube is not limited to a radial width of 8 cm. At the outside radius, the strong support tube is attached by a flange to the yoke supported by the barrel IFR. The inner radius matches that of the assembly flange and the cylinder of the standoff region, which are discussed below. The preferred fabrication method for the strong support tube is to cut slots for the sectors into annular plates of convenient thickness. These are pinned for alignment and held together by as many as 24 axial bolts (12 each on the inside and outside radii).

The 15 cm-deep aluminum assembly flange is rigidly supported from the back of the strong support tube and has two major functions. First, it breaks the magnetic circuit between the standoff region and the poletip, IFR, and strong support tube; and second, it provides the seal and supports for the sectors and standoff regions. Based on the magnetic simulation done to date, it is known that the field at the PMTs is acceptable with the gap; whether it is essential has still to be determined. If it is not, this assembly flange could be eliminated, saving 15 cm in the length of the quartz bars. The strong support tube could handle the major mechanical functions, which would save a significant amount of radial space.

Standoff Region

The standoff volume is filled with approximately six tonne of water, contained by an inner radius cylinder, an outer radius cone at 55°, and a toroidal back PMT support plate. They are of high quality magnetic steel; simulations using 5 cm-thick steel (permeability $\sim 10^4$) gave B $\leq$ 0.05 T at the PMTs with a central field of 1.5 T. Tests on conventional 29 mm-diameter PMTs showed no effect at this field, independent of orientation. It is expected that further optimization through simulation will lead to reduced steel thickness in some regions. In any case, it is essential that the joints between the PMT plate, the cone, and the cylinder provide good flux transfer. With 5 cm-thick walls, the total weight is $\sim$15 tonne. The water reservoir is mounted below the standoff region, so the forces do not change significantly when water is transferred. We plan to use de-ionized reverse-osmosis water, which has an attenuation length of 10 m at $\lambda = 300$ nm. The water will recirculate slowly through a filter and under a UV lamp, and the attenuation will be monitored offline. In addition, there will be an emergency pressure relief valve, an expansion reservoir for temperature changes, and a dam to channel water in case of leaks.

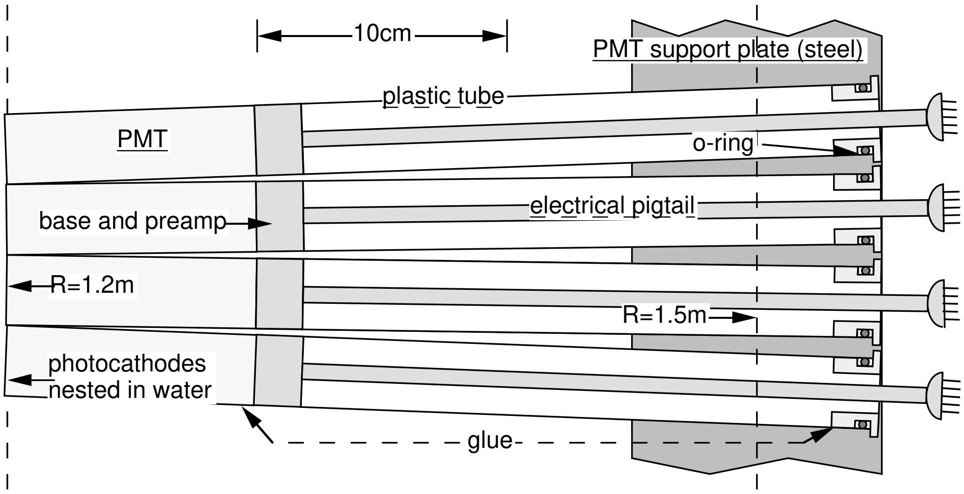

Figure 6-13. *Schematic of a possible PMT module assembly design.*

Mirrors

The mirrors in the standoff region are needed to minimize the required number of PMTs; they have the same azimuthal symmetry as the sectors. The 0° dip angle mirror is essential because half the light from each sector emerges from the quartz bar in a direction which is pointed towards a smaller radius. The mirrors could be aligned from within the standoff volume, although it would be convenient to use sealed adjustments for outside control. The mirrors on the conical surface are presently assumed to be placed at a 55° angle to reduce the number of PMTs.

The mirror design is complicated by the need for immersion in water for a long period of time. If a front surface coating is used, it must be covered for protection. A likely possibility is to use aluminum with a coating of either silicon dioxide or a series of dielectric layers. An alternative is to coat the back of a sheet of thin UV-transmitting quartz, which is then sealed against water. Mirror "coupons" could be immersed in the water circuit and removed periodically to measure the degradation of reflectivity with time. The mirrors will be made neutrally buoyant by using a hexcell support structure to minimize the distortions.

PMTs and Modules

Approximately 13,400 PMTs of 29 mm diameter will be needed to cover the toroidal surface in a close-packed array. The packing fraction depends upon design details but will be $\sim$87%. Typically, the PMTs are only sensitive inside a diameter of 25 mm. To recover this lost region, each PMT will carry a reflecting cone with a depth of 4 mm and radial width 2 mm to collect most of the light hitting the cone at dip angles less than or equal to 30°. The individual PMTs will be mounted into modules that can be joined together to provide a leak-tight interface between the water of the standoff tank and the phototube array. Several different schemes are now under evaluation. One of these is shown in Figure 6-13.

6.4.2 Photodetectors and Readouts

DIRC Readout

In principle, the Cherenkov photon arrival time contains information about the Cherenkov angle. This information becomes competitive with the position information obtained from the array when the time resolution approaches 100 ps for a single photoelectron hit. If cost were not an issue, modern instrumentation and very good PMTs could provide time resolution at this level. However, it is substantially less expensive to determine the angle information from the position on the PMT array plane and not attempt such precise timing. Timing information, however, is still a powerful tool for distinguishing signal from background. For each track, the dominant background comes from the event itself, which occurs over a time window of about 50 ns. Thus, to gain a significant factor in signal to noise on these backgrounds requires a timing resolution of a few nanoseconds. The readout electronics will provide a timing resolution on the order of 1 ns. Although the pulse height carries no additional information for a single hit, it is useful for calibration purposes. We propose implementing a system which offers the option of measuring the pulse height during dedicated calibration runs.

Figure 6-14 is a block diagram of the readout chain for a single PMT. During normal physics running, the time is recorded in a FIFO whenever the signal at the output of the PMT crosses a preset threshold. The FIFO is large enough to store the maximum data for the duration of the Level 1 trigger latency, 9.5 μs. Upon receiving a Level 1 trigger signal, the data in the FIFO falling within a $\pm 0.5\,\mu$s window around the trigger are sent to the DAQ readout module where they are buffered before being shipped over the FDDI network to the Level 3 farm for further processing. The baseline design calls for the front-end electronics to be located near the PMTs, with 64 channels per card and one fiber-optic link to the DAQ readout modules for each group of 960 channels. The VME-based DAQ readout modules, located in the electronics house, will receive four optical fibers each. The baseline design of this system and a description of continuing research are presented in Chapter 10.

Photodetectors and Bases. The criteria of greatest importance for the DIRC photosensors are high quantum efficiency, maximal coverage of the photon image plane, adequate gain, good timing resolution ($\sim$1 ns), low noise, and low cost. The performance of candidate

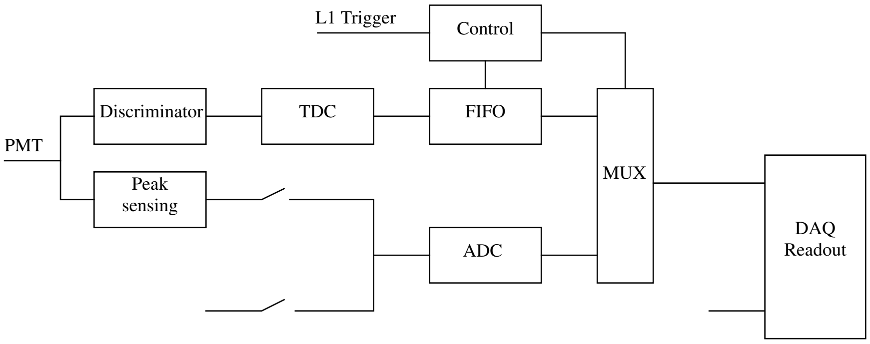

Figure 6-14. *Block diagram of the readout chain for a single PMT. The FIFO is capable of storing data for the duration of the Level 1 trigger latency.*

PMTs from three leading manufacturers has been tested: Hamamatsu R268, Philips XP2982, and EMI 9124A. These PMTs are all of similar design: 29 mm in diameter with bialkali photocathodes. As a result of these investigations, the Hamamatsu R268 has been chosen for the forthcoming prototype with 500 tubes. These tubes are, therefore, included in the DIRC baseline design. The market will be researched again before the final choice of PMTs is made.

Both timing and pulse height information were obtained for the three tube types using a prompt Cherenkov light signal. This was produced by a β particle emitted from a ^{106}Ru source traversing a thin quartz plate. The source was sufficiently weak that nearly all detected signals were the result of single photoelectrons. The absolute gain was derived from the measured pulse height distribution and from the known ADC charge sensitivity. The time distributions were obtained with the same system. A very fast TDC start signal was generated by stopping the β particle in a scintillator. Gaussian fits to these time distributions were used to extract their rms time spread. The noise (dark current) and the photocathode response, were measured. (The latter is defined to be the mean PMT pulse height divided by the gain when the photocathode is uniformly illuminated.) These phototube characteristics, which measure photon detection ability, have been compared for the three tubes using the same light source operated at the same intensity.

The results of the measurements are collected in Table 6-5. The voltages given in the table are the highest voltages at which the PMTs may be safely operated according to criteria which are believed conservative. The dark current can vary from tube to tube and is shown only to indicate that it is small enough to be of no concern. Except for the time resolution, the performance results favor the R268 tube. The improvement in time resolution that would come from using the Philips tube does not compensate for the loss in response.

Tube	HV (kV)	Gain (10^8)	Noise Rate (kHz)	Pulse Height Resol. σ/PH(%)	Time Resol. (ns)	Relative Response
R268	1.6	1.1	2.6	42	1.2	1.6
XP2982	2.0	1.2	3.4	38	0.55	1.0
9124A	2.0	5.7	2.2	20	1.3	1.3

Table 6-5. *Comparison of the three tested PMTs.*

The details of both the electrical and mechanical design of the PMT base depend on the particular device chosen and the mounting scheme. However, neither of these choices poses particularly difficult problems. A base composed of two printed circuit boards has been developed for the current choice of PMT (Hamamatsu R268) in the 500 PMT DIRC Prototype-II. An alternate scheme [Hub92] using a voltage multiplier is also being studied.

The HV feed to 24 individual bases will be provided by a single PC board, serviced by one or two HV supply channels. The same board may also be used to route the signal lines onto a single 24-pair ribbon cable (as with the prototype) or to signal processing electronics on the same board. This board can be mounted directly behind the PMT support.

The PMTs are located in the standoff box. Their backs and bases will be easily accessible for repair and/or replacement.

6.4.3 Laser Flasher Monitoring and Calibration System

The DIRC laser flasher system will be used to measure the gain and relative quantum efficiencies of each tube and to monitor the optical performance of the quartz bars, glue joints, mirrors, and windows. The conceptual design for this system uses one or more pulsed nitrogen lasers as the light source. The wavelength, 337 nm, is characteristic of Cherenkov photons. The pulse duration is shorter than the timing resolution of the DIRC. The number of lasers will be determined by their repetition rate and the desired trigger rate.

The laser light will be distributed by optical fibers. Two methods are under study:

- Locate the fiber between photomultiplier tubes (see Figure 6-15). The light will be directed towards a scattering surface located above the bar window.
- Locate the fibers at the junction of the quartz bar exit and the standoff box with one fiber directed along the bar towards its far side and the other directed into the water through a scattering surface. (The use of LEDs or Xenon flashers in place of lasers is also under study.)

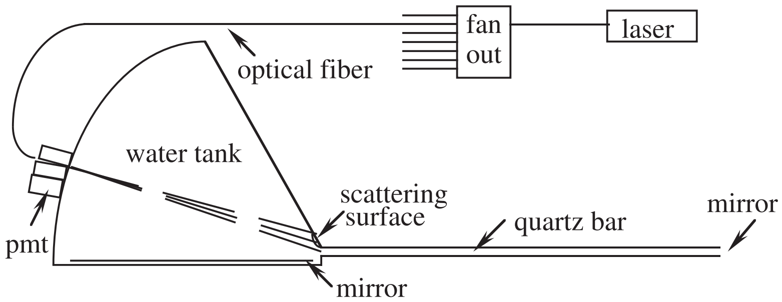

Figure 6-15. *Conceptual design of the DIRC laser flasher system. The 337 nm light is distributed by four fibers per sector and reflected from a diffuse scattering surface, providing a reasonably uniform distribution of single photons to all phototubes.*

Each of the fibers of a sector will be a different length to provide a timing difference that can be used to distinguish pulses from different fibers.

The scattering surfaces will give a reasonably uniform illumination of all phototubes. The light level will be adjusted so that the probability per pulse of any particular PMT being struck by a photon is small. This ensures that essentially all hits will be due to single photoelectrons.

The gain of each PMT will be derived from the single photoelectron pulse height spectrum; the number of hits is a measure of the stability of the relative quantum efficiency.

Light will travel the length of the bar and reflect off the far mirror before striking the PMT. The ratio of the number of these hits to direct hits is proportional to the transmission of the bar, glue joints, window, and the reflectivity of the mirror. The short pulse duration of the light source is needed so that these hits can be distinguished on the basis of timing.

It is anticipated that a flasher calibration will take approximately 10 minutes and be performed once per week. The laser trigger will be used also as a level 1 detector trigger, with a partition for DIRC data only.

6.4.4 Integration Issues

Offline DIRC Assembly and Test

A set of twelve aluminum boxes will be built to simulate the sector boxes containing the quartz bars. These will be dimensionally correct and loaded to the weight of a real sector. These boxes will be preassembled into the central support tube where clearance checks and modifications can, if needed, be made. These boxes will also serve to align the light section of the central support tube with the heavy aluminum section. At this point, the central support tube is rigidly held off the floor by a spider and framework. The central support tube and the strong support tube are mated into an accurate cylinder 5 m long.

The sector boxes will all be installed at the top of the support tube; the support tube will be rotated for each new sector box. We begin by removing a dummy aluminum box and bringing up a sector on an adjustable assembly strongback. The box is precisely aligned with the slot and moves in on rollers pulled by a line. Compressed air flow around the sides reduces friction. After installation, the sector will be sealed to the assembly flange and the next insertion will take place.

The standoff region, which weighs approximately 15 tonne, could be preassembled and moved by crane. A major advantage of this approach is that it would allow an inspection of the PMTs and electronics before moving onto the beam line. At this stage, the weight of the device is supported by the floor. The 24 mirrors in the standoff are installed and aligned, after which the PMT support plate is bolted to the cone. The PMTs and electronics are installed and a dummy assembly flange mounted. The water reservoir and other devices can be attached for calibration, monitoring, and possibly cosmic ray tests.

Online DIRC Installation and Test

The support tube and sector assembly is inserted into the detector, supported by a yoke directly from the barrel IFR. After surveying, shims are used to align the central support tube with the drift chamber. The standoff structure is bolted directly to the assembly flange and sealed. The procedures described above are repeated for inspection and testing and upon successful completion, the beam line elements, poletip, and utilities are placed inside the DIRC tunnel.

Cabling and Access

The signals from the 13,400 DIRC phototubes are carried by ribbon wax or twisted pair cables to the front-end electronics, located in nearby crates. They are multiplexed onto a small number of optical fibers for transmission to the electronics hut. The cable plant is dominated by the ~900 HV cables. There are, in addition, 144 optical fibers for calibration and additional cables for monitoring and charge-injection calibration. The cable routing is straightforward and presents no interference to other systems.

All active components of the DIRC are located in the standoff box and can be accessed by removing the electronics covers—no other detector subsystems must be moved. Access is expected to be required infrequently, since the failure of a small number of isolated channels will have no impact on the physics performance. No access is required to the radiators.

6.4.5 Research and Development Program

Prototype-I: Proof of Principle

The goal of the conceptual prototype (Prototype I) was to demonstrate the basic proof of principle of the DIRC [Ast94]. Because no detector like the DIRC had been built before, this prototype needed to address many fundamental issues, and be easily modified to respond to new issues that arose during the studies. The detector was placed in a cosmic ray beam hardened to 1 GeV/c by an iron stack. A series of scintillation counters served as the trigger, and a set of straw tube chambers was used for tracking in the angular resolution studies. The quartz bar used initially was $120 \times 4.7 \times 1.7\,\mathrm{cm}^3$. It was supported at a few contact points inside a light-tight box. Later, two bars were glued together to make a bar 240 cm in length. A mirror was attached to the non-readout end in order to make studies at an effective distance of 4 m from the readout end in the reverse configuration. For the photoelectron yield and attenuation length studies, a Burle 8850 51 mm PMT was glued to the end of the bar. For the angular resolution measurements, an array of 47 EMI 9124A 29 mm PMTs was placed at varying distances from the end of the bar with air filling the standoff region.

The photoelectron yield was studied as a function of dip angle and position along the bar. The results of one of these measurements are shown in Figure 6-16, for a position in the middle of a bar. These results are consistent with the Monte Carlo prediction, shown as a solid line. The behavior at large dip angles demonstrates a major advantage of the DIRC at an asymmetric collider in that the highest momentum tracks, which are forward-going at large dip angles, produce large numbers of photoelectrons. The measured yield with the PMT directly glued to the bar does not represent the number expected in the real DIRC at the same distance and angle, since there are additional losses from the packing of the array tubes, water in the standoff region, and transition effects.

There are also length-dependent losses from attenuation in the quartz, both from light absorption in the bulk material, and from losses at the surface. To study these effects, a series of measurements was made with both the 120 and 240 cm bars, in both forward and mirror reflected configurations at a constant dip angle. As expected, when characterized by a simple exponential, the measured attenuation lengths become somewhat longer as the path lengths increase. However, with this readout system, they are approximately 10% per meter, consistent with a bulk transmission length of greater than 10 m, and an internal reflection coefficient of more than 0.9995. This performance, which is completely adequate for the DIRC needs of *BaBar*, is shown in Figure 6-5.

The single photoelectron angular resolution was studied for a variety of dip angles, positions of the beam along the bar, and standoff distances in air. Major contributors to the resolution are source and detector size, and chromatic dispersion. Lesser contributions come from the momentum spread in the beam, multiple scattering, tracking, and reconstruction errors

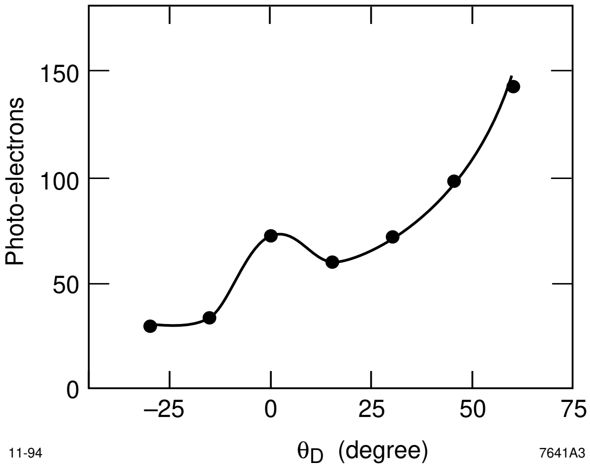

Figure 6-16. *Observed photoelectron yield from a 1.7 cm-thick DIRC bar at a track position 60 cm from the photodetector end as a function of the track dip angle θ_D. The solid line is a Monte Carlo simulation; the statistical errors are smaller than the data points. There is a scale error of 3% due to calibration uncertainty.*

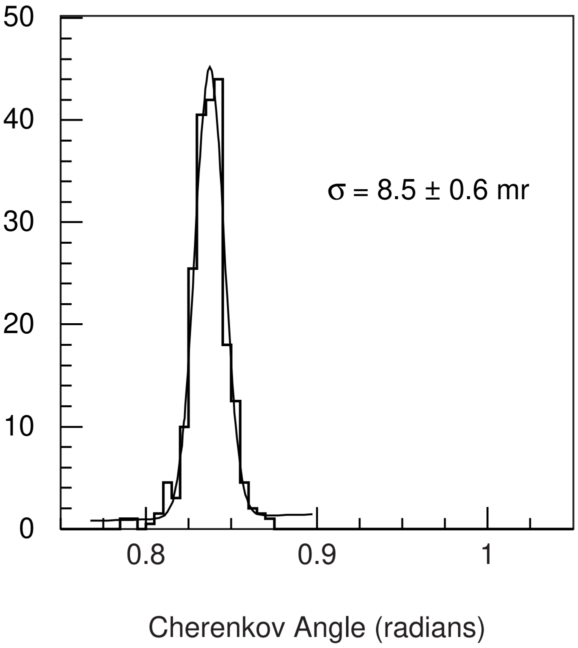

Figure 6-17. *Single Cherenkov photon angle distribution at $\theta_D = 30°$, a standoff distance of 90 cm, and a track position 205 cm from the end of a 240 cm-long bar. The line shows a fit to the data obtained with a Gaussian plus polynomial form.*

in the telescope. A typical result is shown in Figure 6-17. The measurement resolution of 8.5 $\pm$ 0.6 mr is in good agreement with Monte Carlo simulations for the Prototype-I configuration, but differs from the resolution which will be obtained with the actual DIRC.

In addition to the cosmic ray tests, a test in a proton beam was performed using a quartz bar identical to the one described above. A PMT was attached directly at each end of the bar with a silicone optical joint, and both amplitude and timing information were recorded. Proton beams of $\beta = 0.8$ and 0.95 traversed the quartz bar at various positions and angles along the quartz length. The number of photoelectrons detected by the PMT, towards which the emitted Cherenkov light propagates by internal reflection, was measured to be 65 for $\beta = 0.95$ at a 30° angle of incidence. The observed absorption was only 3% per meter. The fact that the number of photoelectrons was slightly smaller and the absorption length longer than in the cosmic test is thought to be due to the different absorption properties of the optical couplers between the bar and PMT.

A significant amount of light was also detected by the opposite PMT. The direction and speed of propagation of this light has been measured, and two components have been clearly identified. The first corresponds to reflection from the other PMT of the normal Cherenkov light. In this setup, its fraction amounted to 8% of the emitted light.

The second component cannot be produced by Cherenkov emission of the incident particle since it travels in the wrong direction, with a low longitudinal propagation speed that does not depend on the incident track angle, and is seen even below the Cherenkov propagation threshold. This second component, produced isotropically in the bar, was present in approximately 30% of the events and corresponded to about four photoelectrons (with an exponentially falling amplitude spectrum). In *BaBar*, this component will lead to an extra background of 2 to 3 photoelectrons per track, if a simple extrapolation holds, and therefore will not degrade the DIRC performance.

The conceptual prototype test program, which is now completed, was essential as the proof-of-principle test, demonstrating that the DIRC can produce enough photoelectrons with sufficient angular resolution for all track angles and positions to provide good π/K separation for *BaBar*.

Prototype-II: Large-Scale Engineering Prototype

After the proof of principle, the next important step is a proof of viability for a large, complete detector system. To that end construction is nearing completion on a large scale prototype (Prototype-II), which approximates a full size section of the eventual configuration. It provides a realistic model to test many of the principal engineering and fundamental system performance issues. In particular, it will allow the observation of a nearly complete Cherenkov image on a track-by-track basis and the direct measurement of the resolution, in mass or $\Delta\beta$, also on a track-by-track basis. Moreover, because of its size, the prototype provides a realistic assessment of the impact of the mechanical structure on the performance of the final device. Examples of components which may affect performance are glue joints between bars, quartz windows, water-filled standoff box, mirrors, PMTs, supports, and interface.

A cut-away isometric view of Prototype-II is shown in Figure 6-18. The prototype consists of two $1.67 \times 4.6 \times 120$ cm quartz bars glued together to form a composite bar 240 cm long. This bar is coupled to a water-filled standoff region with one mirror inside and 500 PMTs (29 mm in diameter) on the back plane of the standoff region for photodetection. The phototubes are read out into standard modular electronics.

The dimensions of the standoff box are 2.4 m wide by 1.2 m on each edge, with a 60° angle between each of the large surfaces. There are two possible ports at which the quartz bar can be connected to the standoff box, one centered and one off center. The latter port allows

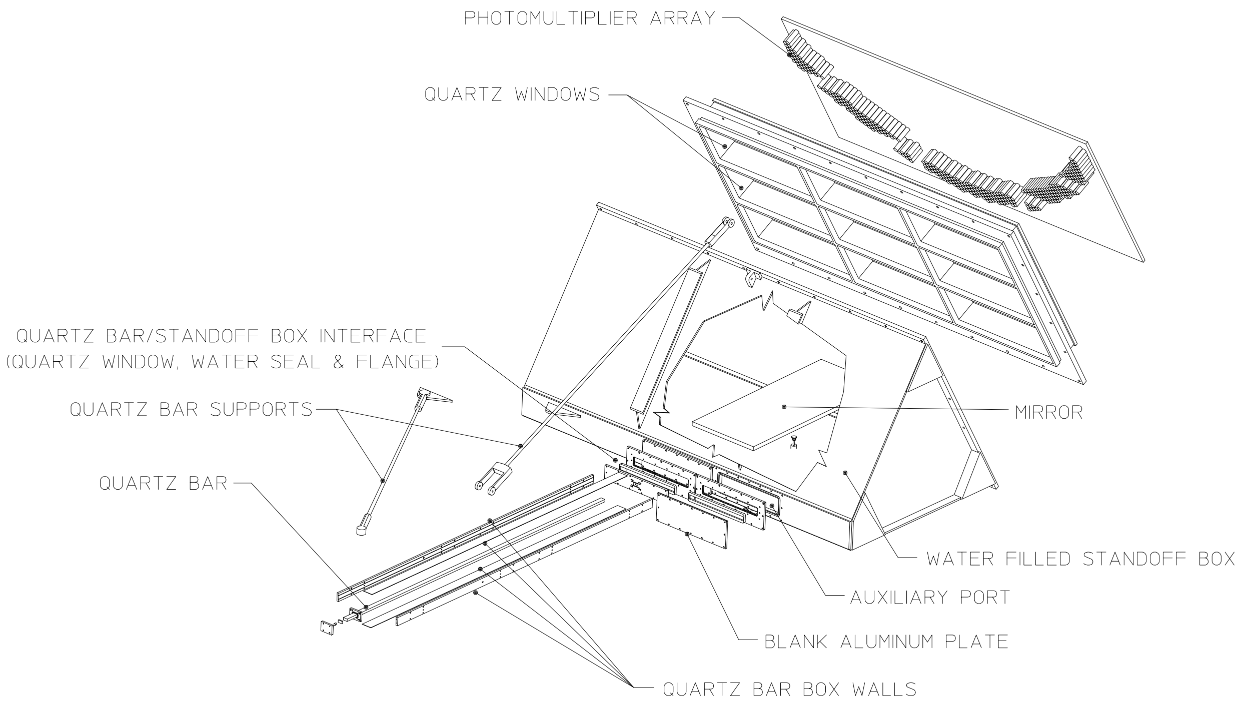

Figure 6-18. *Isometric view of the Prototype-II detector.*

the study of the extreme end regions of the Cherenkov conic images outside the acceptance of the back plane when the quartz bar is in the center port. The quartz bar is connected to the port by an interface consisting of a quartz window sealed in a watertight frame bolted to the standoff box. The port and interface are the same size as in the final configuration, which will accommodate a complete sector of quartz bars.

For simplicity, the back surface is a plane, instead of a curved toroidal shape, in the final configuration. Because of the limited number of PMTs for the prototype, they must be specially configured on the back plane for each beam dip angle to subtend the specific band of light corresponding to the Cherenkov image produced at that angle. To provide maximum flexibility for this, the PMTs are separated from the water volume by a 2 cm-thick quartz window barrier, made up of nine window panes as shown.

Construction of Prototype-II at LBL is scheduled for completion at the end of February, 1995. It will then be installed in a hardened cosmic ray telescope at SLAC for tests from March through early May. It will then be shipped to CERN for extended tests starting in early June of 1995, with beams of pions, kaons, and protons below about 4 GeV/c.

Future upgrades of this prototype will include lengthening the quartz bar to 480 cm, attaching bar mirrors, adding more bars side by side (up to 12) to make up a quartz bar sector as in

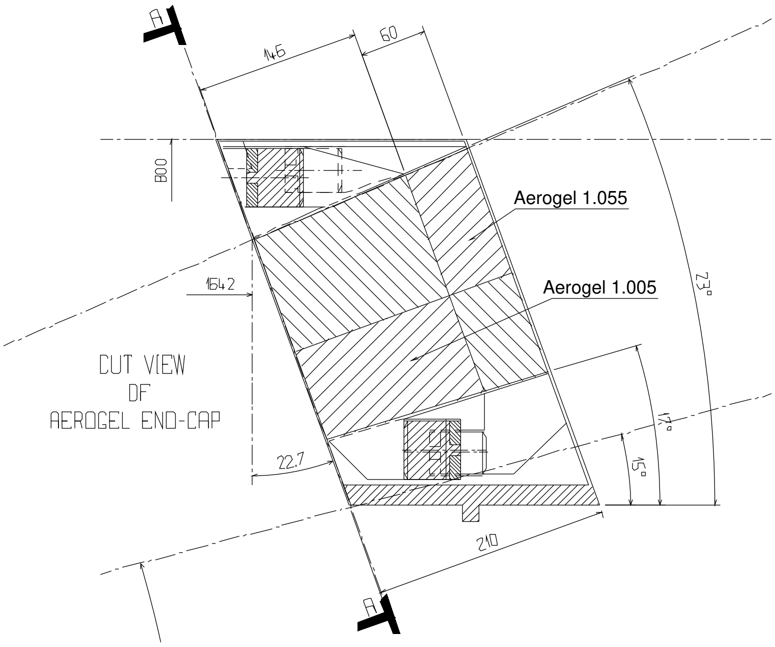

Figure 6-19. *R-θ view of the ATC detector*

the final configuration, adding more PMTs, testing various calibration schemes and different electronics. The versatility of this prototype construction also permits future tests of different PMT mounting and interface schemes with the water volume, such as having the PMT front faces immersed in the water.

6.5 The ATC Detector

6.5.1 ATC Mechanical Design

The forward PID system consists of 144 blocks of aerogel arranged in two rings that are two layers deep, as shown in Figures 6-19 and 6-20. The front layer, 146 mm long, has a refractive index of ~ 1.006, and the back layer, 60 mm long, has an index of ~ 1.055. The detector will be built in two C-shaped pieces, as shown in Figure 6-21, as is the endcap electromagnetic calorimeter, to which it is attached.

Each half endcap is composed of:

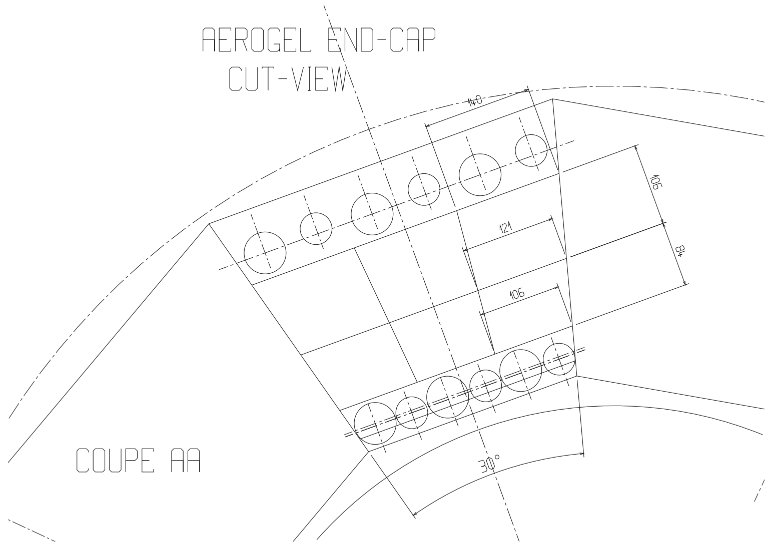

Figure 6-20. *R-ϕ view of one ATC module.*

- Six modules, subtending 30° in ϕ, each housing six aerogel blocks of two indices. The block dimensions are shown in Figure 6-20. The modules, shown in Figure 6-21, are made of a light composite material covered by a water-resistant PTFE Teflon with a reflectance of about 95% over the region 300–700 nm. PTFE teflon has been used extensively in our beam tests. Any diffuse reflector used for the aerogel wrapping must be of low density and high reflectivity. It must remain stable over a long period. Other candidates are Millipore paper and Kodak paint. All are hydrophobic and commercially available. Reflectivities of these materials are under study.

- Each aerogel block is read out by a Hamamatsu fine mesh photomultiplier through a diffusing box located on the top and bottom of the module, as shown in Figure 6-19. Phototubes of 52 and 35 mm diameter are used for the 1.0065 and 1.055 blocks, respectively. The effect of the material in the phototube on the performance of the DIRC and calorimeter is being studied.

- The modules are glued on a half cone skin made of 2 mm-thick composite material. This front skin supports kapton high voltage and signal cables.

- The entire front section, equipped with readout and aerogel blocks, is mounted inside a conical backing structure arranged as a half-shell in azimuth. This support provides rigidity for each half endcap, supports cables and services, prevents light leaks between cells, and provides the mechanical connection to the supporting calorimeter endcap.

Generated heat is removed by blowing nitrogen at the top and bottom of the detector around all tubes. The nitrogen flow also protects the aerogel against humidity.

The size of the aerogel blocks is a compromise between minimizing the number of readout channels and maximizing the number of photoelectrons. A low-density block of transverse size $10 \times 10\,\mathrm{cm}$ has been demonstrated in a test beam to have acceptable performance. A block of this size at 170 cm from the interaction point corresponds to a 3.2° angle. Only 2.1% of kaons overlap with another charged particle within this angular range. This fraction drops to 0.4% for a 1.6° cone, corresponding to the case in which two particles fall in the same block, whatever the impact point. Larger block sizes also lead to poor and nonuniform photon collection. Simulations show that going from a $10 \times 10\,\mathrm{cm}^2$ to a $10 \times 20\,\mathrm{cm}^2$ block reduces the average number of photoelectrons by a factor of 3. For these reasons, a $10 \times 10\,\mathrm{cm}$ transverse block dimension has been adopted for the baseline design.

6.5.2 Photodetectors and Readouts

In order to collect Cherenkov photons efficiently inside the solenoid, the photon detector must work in magnetic fields of up to 1.5 T, have a large UV sensitive area with high quantum efficiency, and have low noise. The baseline design uses 19-stage fine mesh photomultiplier tubes (FM PMT) from Hamamatsu with a newly developed high quantum efficiency bialkali photocathode. Hamamatsu's FM PMTs with a conventional bialkali photocathode have been widely used in high-energy experiments [Gil88]. The newly developed FM PMT gives much higher quantum efficiency (see Figure 6-22). Using the new FM PMT, $\sim$1.7 times as many Cherenkov photons were observed from a prototype aerogel counter in our beam test at the KEK PS facility than were observed with an older version.

Our recent studies using a spectrometer magnet at SLAC [Gea94] confirm that a conventional 16-stage FM PMT has a gain of 4×10^5 at 1.5 T, if tilted at 45° with respect to the field [Kic93, Suz86, Ham94]. At $\sim 5^\circ$ the relative gain drops by factor of $\sim$200 for 1.35 T, as shown in Figure 6-23. Without the magnetic field, the FM PMT has a gain on the order of 10^7, an intrinsic excess noise factor (ENF) of $\sim$2 due to the inefficiency of the mesh dynode structure, and negligible electronic noise. When operated in a magnetic field, the FM PMT's gain drops substantially, its effective ENF increases due to the influence of the field on electron trajectories in the tubes, and the overall electronic noise increases because an amplifier is needed to increase the signal. As a consequence, even though the FM PMT gives the highest gain at a 45° angle to the magnetic field, an optimal operation angle must be determined for single photon response. A series of tests have been performed which indicate that a 2″ FM PMT tilted $\sim 5^\circ$ with respect to the field gives a reasonable photoelectron yield along with an optimal pedestal-to-signal separation for the aerogel counter readout.

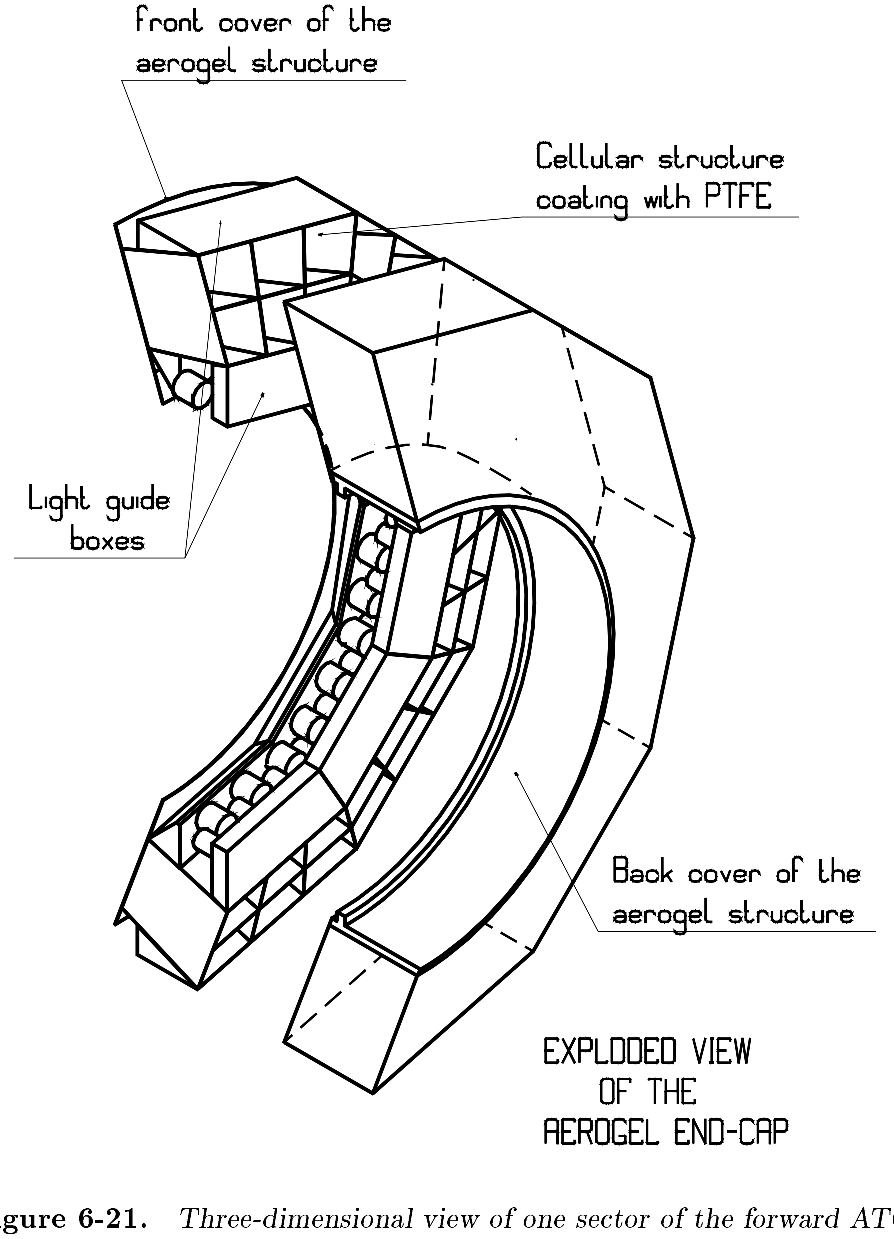

Figure 6-21. *Three-dimensional view of one sector of the forward ATC.*

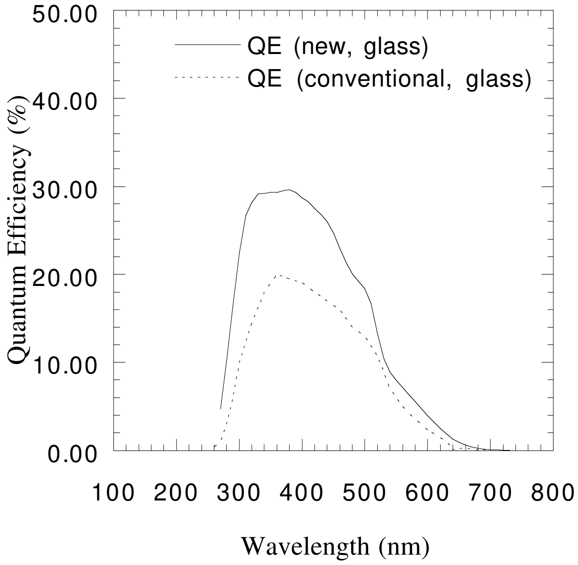

Figure 6-22. *Comparison of the quantum efficiency of the newly developed fine mesh PMT (solid line) vs. a conventional PMT (dashed line). Both PMTs have glass windows.*

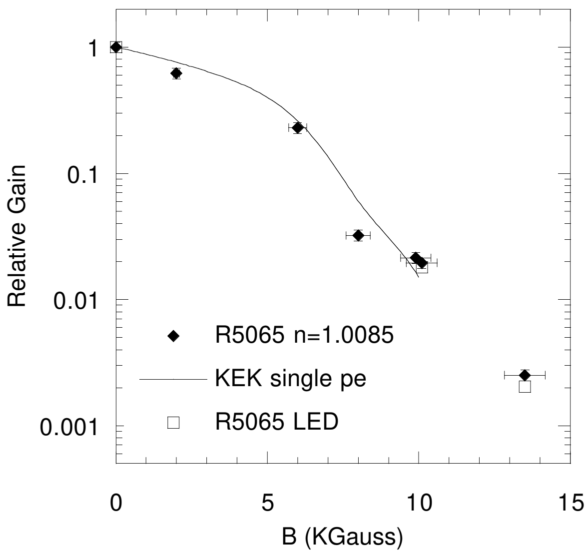

Figure 6-23. *Measured relative gain of a fine mesh PMT operated in magnetic fields up to 1.35 T.*

More compact readout devices, such as hybrid photodiodes (HPDs) and microchannel plates (MCP PMTs) are also being considered. The characteristics of HPDs and MCP PMTs, and their performances in magnetic fields, have been extensively studied by the aerogel PID group and by others at KEK, DESY [Kic93, Suz86], and CERN [Des94a]. An outline of their characteristics is provided here. More detailed descriptions can be found in Section 6.5.5.

The HPD has the advantage of being a ENF$\sim$1 photon detector, while its overall effective electronic noise is on the order of a few photoelectrons. Its low gain, $\sim 3 \times 10^3$, requires the use of a charge-sensitive amplifier. However, the overall effective electronic noise has been reduced to less than or equal to 1 photoelectron in a recent test. The improvement in the signal-to-noise ratio of the HPD comes from using a photodiode with a thicker depletion layer, applying more voltage in the vacuum gap, and reducing the thickness of the inactive layer in front of the photodiode [Des94b]. Improving the HPD's performance has been one of our major R&D efforts.

Newly developed GaAsP micro-channel plate photomultiplier tubes (MCP PMT) from Intevac have quantum efficiencies of $\sim$10% at 350 nm and $\sim$40% at 500–600 nm [Edg92], providing a better average collection efficiency for Cherenkov light than FM PMTs. The

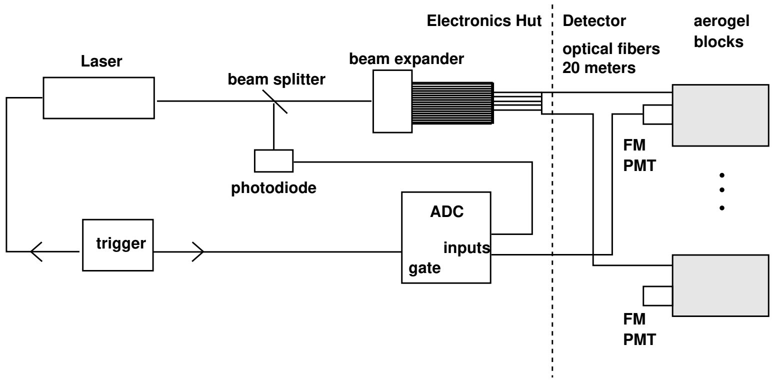

Figure 6-24. *Conceptual design of the ATC laser flasher system.*

MCP PMT has a gain on the order of 10^6, an ENF measured to be $\sim$1.4, and is immune to magnetic fields [Kic93]. The Novosibirsk Institute of Semiconductor has successfully produced an InGaAsP MCP PMT with a quantum efficiency of $\sim$50% at 600 nm [Alp94].

6.5.3 Monitoring and Calibration System

A laser-driven optical fiber will be attached to each aerogel block to monitor the stability of the aerogel and photodetector on a short term basis. The system will use a pulsed nitrogen laser, which has a 337 nm wavelength. The laser beam is optically split into two beams: one is monitored by a photodiode to determine the stability of the laser pulse, and the second is expanded and coupled into an optical fiber which is attached to the back of each aerogel block (Figure 6-24). The long-term calibration of the system will be performed using Bhabha events, dimuons, and pions from K_S^0 decays.

6.5.4 Integration Issues

ATC Assembly, Installation and Test

After positioning and gluing the six modules of each endcap segment, the cells are filled with the aerogel blocks, and photodetectors are mounted inside the diffusing boxes. Bases and pre-amplifiers are also mounted during this operation. The detector is closed by attaching the back cover of the aerogel structure. Each half endcap is assembled and transported independently. Special tools have to be developed for positioning and gluing the modules.

Each ATC endcap is mounted on the front face of the endcap calorimeter, and aligned with respect to it, before installing the two detectors.

Cabling and Access

The front-end electronics for the ATC are situated on the detector, and for any access to this part, the ATC and the electromagnetic endcap calorimeter have to be removed. After dismounting the back cover of the aerogel structure, access to all electronics and aerogel blocks is possible.

Cables from the detector to the DAQ, which is located outside the *BaBar* detector, run between the beam pipe and the inner radius of the ATC.

6.5.5 Research and Development Program

Prototype Beam Test Results

Proof-of-principle requirements have been met through several beam tests of prototype aerogel counters read out with fine mesh photomultipliers in a strong magnetic field at CERN and KEK. More than 10 photoelectrons have been observed with both $n = 1.0085$ and $n = 1.063$ aerogel counters. Threshold curves have been mapped out, and 4σ separation between below threshold particles and above threshold particles has been obtained. In magnetic fields up to 1.0 T, 13 photoelectrons were measured when a 5 GeV/c charged pion traversed a masked 3″ fine mesh PMT with a UV window and a sensitive diameter of 44 mm.

Both $n = 1.0085$ and $n = 1.063$ aerogel counters with sizes of $10 \times 10 \times 10$ cm and $10 \times 10 \times 4$ cm, respectively, were wrapped with eight layers of 1.5 mil PTFE covered with a thin layer of aluminized mylar and placed into the beam. Minimum ionizing particles were selected by four scintillation trigger counters and identified by two CO_2 gas Cherenkov counters operated at about 3 atm. A lead brick with a thickness of 2 cm, corresponding to $3.6X_0$, was placed behind the aerogel counter, between the fourth trigger counter and a veto counter, to veto electrons as well as to simulate backsplash from the calorimeter.

Light yields of 9.2 photoelectrons were obtained by reading out the $n = 1.0085$ counter with a 2″ RCA Quantacon PMT (C31000M); 10.2 photoelectrons were obtained from the $n = 1.063$ aerogel counter by a masked RCA Quantacon PMT with effective sensitive diameter of 27 mm. The momentum-dependence of the light yield demonstrates that both aerogel counters behaved as threshold Cherenkov devices, as shown in Figure 6-25. The measured refractive indices 1.0087 ± 0.004 and 1.061 ± 0.005 were in good agreement with the refractive indices provided by the aerogel manufacturer, 1.0085 and 1.063, respectively.

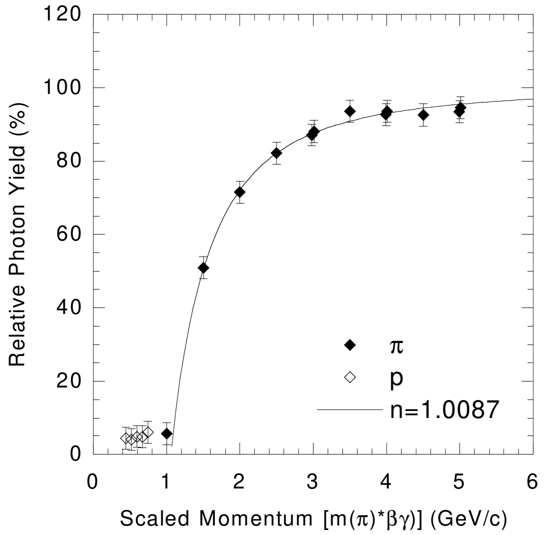

Figure 6-25. *Measured threshold curves of the aerogel Cherenkov counters.*

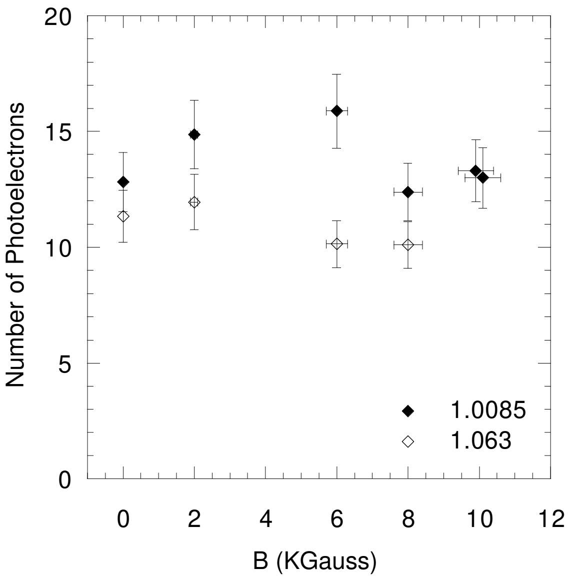

Figure 6-26. *Photoelectron yield of the aerogel counters read out by fine mesh PMT's in the magnetic field.*

The aerogel detectors were also read out by fine mesh PMTs operated in magnetic fields up to 1.0 T. The setup is very similar to the beam tests described above, except that the aerogel counters were sandwiched between two $10 \times 10 \times 10$ mm trigger counters placed inside the magnet to have a better determination of the path of charged particles in the field. The 1.06 aerogel counter used in this beam test is the same as the one used in the previous test, while the dimensions of 1.0085 aerogel counter were changed to 12 cm long and 10×8.5 cm in transverse dimensions. The photoelectron yields of $n = 1.0085$ and $n = 1.063$ aerogel counters at different magnetic fields are summarized in Figure 6-26.

Another beam test of the prototype 1.0085 aerogel counter was carried out at the KEK PS test beam facility. Sixteen photoelectrons were measured for 3.5 GeV/c charged pions using a newly developed fine mesh PMT with a glass window and an effective sensitive diameter of 44 mm in a 1.3 T field. This corresponds to a light yield of 18 photoelectrons for $\beta = 1$ particles. A clear separation of the above and below threshold particles was obtained, Figure 6-8. The uniformity of the light collection efficiency was also studied in the $n = 1.0085$ aerogel counter by running the beam at various transverse positions across the counter. The average light yield is plotted as a function of the distance from the beam to the PMT in Figure 6-27. The measured response is determined to change by less than 12% over a 4 cm distance.

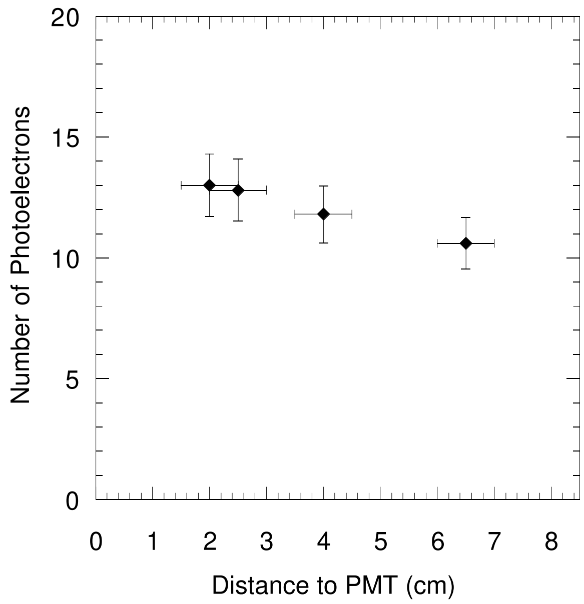

Figure 6-27. *Uniformity of the light collection efficiency.*

The HPD option

The proof of principle that an aerogel-counter-based PID system can work efficiently in the *BaBar* environment, namely that more than ten photoelectrons are read out in a magnetic field of 1.5 T has been obtained using Fine Mesh PMTs. There are, however, good reasons to continue the investigation of other photon detector candidates. Among them, the most promising seems to be the Hybrid Photodiode (HPD) because of its substantial immunity to magnetic field effects, its wide angular acceptance and its extreme compactness (25 mm total length).

The HPD tube consists of a normal photocathode coupled to an anode made out of a silicon photodiode separated by a thin vacuum gap. An incoming photon is converted into a free electron at the photocathode, accelerated toward the silicon diode, and stopped in the depletion volume. A gain of about 3000 is achieved for a 15 kV electric field. The charge is collected on the anode and read out on a charge preamplifier.

Results of measurements in a magnetic field. Several 1″ diameter HPD tubes have been tested in a magnetic field. The tubes were operated at 8 kV. A simple setup allowed variation of the angle between the HPD axis and the field direction with a precision of about 1–2 degrees. A green LED attached to the HPD was used as the source of light.

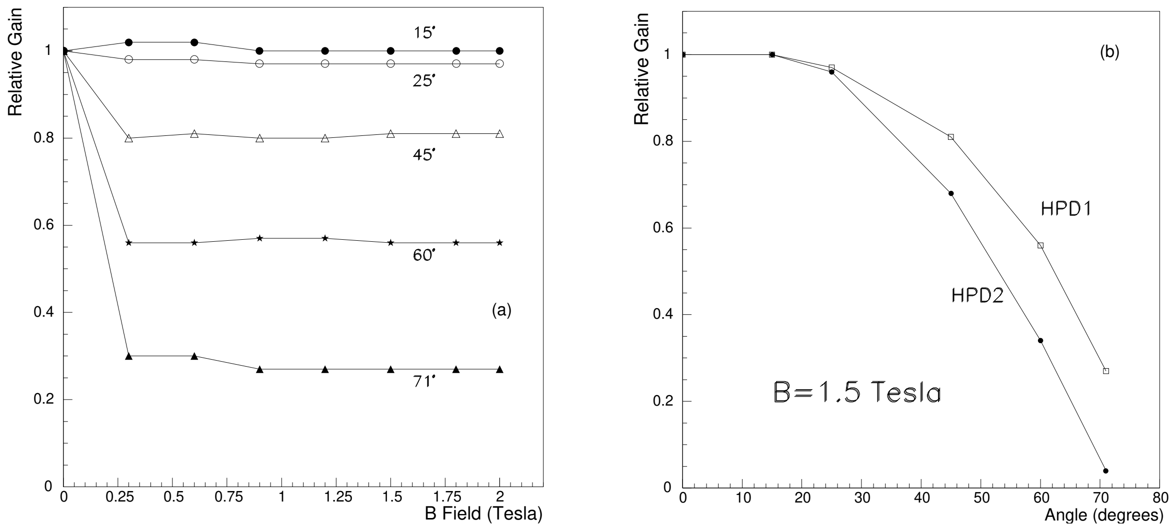

Figure 6-28. *(a) HPD response versus magnetic field for a tube with a 5.6 mm gap; (b) HPD response versus angle with the field for two tubes with different gaps.*

A scan in angle was performed, at values between 0° and 71° and at different values of the field between 0 and 2 T [Cal95]. The results of these measurements are given in Figure 6-28. From these measurements it is clear that HPDs show no loss of signal in magnetic field at 0° angle, and a small decrease at higher angles (~30% at 45°–50°, depending on the individual device).

To find the optimal parameters for an HPD tube to be used as an aerogel photon detector we intend to perform a series of laboratory tests in close contact with the manufacturer. A potential of about 15 kV will be used to operate the tubes in order to increase the gain and thereby reduce the importance of the electronic noise. However, it has yet to be demonstrated that 15 kV is possible without extending the gap between photocathode and anode beyond 5–8 mm and without any induced noise on the diode and the preamplifiers. Other parameters, such as diode thickness (relevant for noise) and window thickness, must also be optimized. We expect to receive the final tube design by the spring of 1995; in the meantime, several prototypes that are already available will be tested in the laboratory, using LEDs and aerogel cosmic rays tests, to evaluate progress.

Tests at CERN

In 1995 we plan a test of all elements needed for the final choice of the detector configuration using a beam at CERN. In particular, aerogel blocks from different suppliers and a variety of photon detectors and preamplifiers will be studied. Based on these results, we plan to build a full (30°) section of the ATC module at the beginning of 1996 and test it in a beam of pions, kaons, and protons to study all aspects of the detector performance in a realistic environment.

References

[Alp94] V. Alperovich *et al., Nucl. Instr. Methods* **A340**, 429, (1994).

[Ast94] D. Aston *et al.,* "Test of a Conceptual Prototype of a Total Internal Reflection Cherenkov Imaging Detector (DIRC) with Cosmic Muons," SLAC–PUB–6731, (1994).

[Ben91] B. Bencheikh, R. DeSalvo, W. Hao, C. Xu, and K. You, "A Simple Light Detector Gain Measurement Technique," CERN–LAA–HC/91–007, (1991). CERN–PPE/91–143, (1991).

[Cal95] M. Calvi *et al.,* "Hybrid Photodiode Performance in High Magnetic Field," *BaBar Note* # 208 (1995)

[Des94a] R. DeSalvo *et al.,* CERN–LAA/HC/94–04 (1994); CERN–PPE/93–101 (1993), DEP Scientific Technical Information (1993); *DIRC R&D Plans*, Internal Note, Paris (1994).

[Des94b] R. DeSalvo, private communication.

[Edg92] J.P. Edgecumbe *et al.,* Proceedings of SPIE (1992).

[Gea94] Magnet was provided and operated by R. Gearhart, SLAC.

[Gen92] P. Bailly and J.-F. Genat, "A 100 Picosecond Resolution, 6 Microsecond Full Scale Multihit Time Encoder in CMOS Technology," Proc. of the Third Int. Conf. on Electronics for Future Colliders, Chestnut Ridge, 57 (1993).
See also: J.-F. Genat, "High Resolution Digital Time to Digital Converters," Proc. of the First Int. Conf. on Electronics for Future Colliders, Chestnut Ridge, (1991).

[Gil88] T.T. Giles *et al.* (CLEO-II), *Nucl. Instr. Methods* **A252**, 41 (1988); S. Ahmad *et al.* (STAR), *Nucl. Instr. Methods* **A330**, 416 (1993).

[Gro92] J.E. Grove *et al., Nucl. Instr. Methods* **A314**, 495 (1992).

[Ham94] Hamamatsu, private communication.

[Hru94] L. Hrubesh, LLNL, private communication.

[Hub92] L. Hubbeling, "Large Photomultiplier Systems–A New Approach," CERN-Preprint ECP 92–10, (1992).

[Kic93] H. Kichimi *et al., Nucl. Instr. Methods* **A325**, 451 (1993).

[Men94] D. Mendez, Lockheed, private communication.

[Oya94] J. Oyang, *BaBar Note* # 137 (1994).

[Pur93] Purschke *et al.,* "A New High Voltage Supply for Large Photomultiplier Systems," International Conf. on Electronics for Future Colliders, CERN Preprint, (1993)

[Rat92] B. Ratcliff, *BaBar Note* # 92; P. Coyle *et al.,* "The DIRC Counter: A New Type of Particle Device Identification for the B Factory," *Nucl. Instr. Methods* **A343**, 292 (1994).

[Shi94] X. Shi, *BaBar Note* # 142 (1994). "Status Report on the Design of a Detector for the Study of *CP* Violation at PEP-II at SLAC," SLAC–419 (1993).

[Suz86] S. Suzuki *et al.,* IEEE Trans. Nucl. Sci. **NS-33**, 377 (1986); H. Saito *et al., Nucl. Instr. Methods* **A270** (1988) 319; J. Janoth et al., DESY 93–119 (1993).

[Tso94] Dr. Tsou, JPL, private communication.